

Roles of Localized Electronic Structures Caused by π Degeneracy Due to Highly Symmetric Heavy Atom-Free Conjugated Molecular Crystals Leading to Efficient Persistent Room-Temperature Phosphorescence

Shuzo Hirata

Conjugated molecular crystals with persistent room-temperature phosphorescence (RTP) are promising materials for sensing, security, and bioimaging applications. However, the electronic structures that lead to efficient persistent RTP are still unclear. Here, the electronic structures of tetraphenylmethane ($C(C_6H_5)_4$), tetraphenylsilane ($Si(C_6H_5)_4$), and tetraphenylgermane ($Ge(C_6H_5)_4$) showing blue-green persistent RTP under ambient conditions are investigated. The persistent RTP of the crystals originates from minimization of triplet exciton quenching at room temperature not suppression of molecular vibrations. Localization of the highest occupied molecular orbitals (HOMOs) of the steric and highly symmetric conjugated crystal structures decreases the overlap of intermolecular HOMOs, minimizing triplet exciton migration, which accelerates defect quenching of triplet excitons. The localization of the HOMOs over the highly symmetric conjugated structures also induces moderate charge-transfer characteristics between high-order singlet excited states (S_m) and the ground state (S_0). The combination of the moderate charge-transfer characteristics of the S_m - S_0 transition and local-excited state characteristics between the lowest excited triplet state and S_0 accelerates the phosphorescence rate independent of the vibration-based nonradiative decay rate from the triplet state at room temperature. Thus, the decrease of triplet quenching and increase of phosphorescence rate caused by the HOMO localization contribute to the efficient persistent RTP of $Ge(C_6H_5)_4$ crystals.


1. Introduction

Room-temperature phosphorescence (RTP) is used in organic light-emitting diodes,^[1-4] photodynamic therapy,^[5,6] in vivo imaging,^[7] and sensing applications.^[8] The highly efficient RTP from heavy-atom complexes is caused by a fast radiative process from the lowest triplet excited state (T_1).^[1-8] In contrast, the

radiative rate from T_1 (k_p) of heavy atom-free conjugated structures is small. In addition, the nonradiative rate of intramolecular vibrational relaxation at room temperature (RT) from T_1 ($k_{nr}(RT)$) and the triplet quenching rate at RT caused by interactions with the ambient surroundings ($k_q(RT)$) are often much larger than k_p . Therefore, reports of RTP from heavy metal-free aromatic molecules under ambient conditions have been scarce.^[9,10] In the last five years, the fast nonradiative processes from T_1 have been suppressed in a variety of heavy atom-free conjugated molecules under ambient conditions, which has allowed electrons in T_1 to partly access the slow RTP pathway.^[11-17] Because heavy atom-free molecules with T_1 with strong $\pi\pi^*$ characteristics have very small k_p ,^[18] RTP from such conjugated structures exhibits persistent emission characteristics.^[12-17] Persistent emission characteristics from such materials could be used in small-scale and cost-effective 2D photodetectors.^[19] Therefore, these materials are potentially useful for a variety of applications, such as thermometers,^[20] security,^[13,15,21-24] stimuli sensors,^[25,26] optical recording,^[27-29] and bioimaging,^[28,30,31] which are independent of autofluorescence. In 1939, Clapp reported that tetraphenylmethane ($C(C_6H_5)_4$), tetraphenylsilane ($Si(C_6H_5)_4$), and tetraphenylgermane ($Ge(C_6H_5)_4$) as nonpolar highly symmetric aromatic molecular crystals showed persistent RTP under ambient conditions.^[9] Since then, persistent RTP has been observed under vacuum or inert conditions but disappeared under ambient conditions for some other aromatic structures.^[32-38] Except for a few reports before 2000,^[9,10] persistent RTP characteristics under ambient conditions have been observed recently from heavy atom-free isolated conjugated molecules doped in a highly rigid amorphous host^[12,20,21,39-41] and crystalline host,^[42,43] carbon nanodots,^[13,22-24,44,45] heavy atom-free aromatic crystals,^[14-16,25,26,46-52] metal-organic frameworks,^[17,53] and nonconventional luminogens.^[54,55]

Considering host-guest materials, in 2013 we reported efficient red-green-blue persistent RTP with more than 10% efficiency from heavy atom-free conjugated structures doped

Prof. S. Hirata
Department of Engineering Science
University of Electro-Communications
1-5-1 Chofugaoka, Chofu, Tokyo 182-8585, Japan
E-mail: shuzohirata@uec.ac.jp

 The ORCID identification number(s) for the author(s) of this article can be found under <https://doi.org/10.1002/adv.201900410>.

© 2019 The Author. Published by WILEY-VCH Verlag GmbH & Co. KGaA, Weinheim. This is an open access article under the terms of the Creative Commons Attribution License, which permits use, distribution and reproduction in any medium, provided the original work is properly cited.

DOI: 10.1002/adv.201900410

into highly rigid short conjugated host molecules under ambient conditions.^[12] In the host–guest molecular materials, the highly rigid short conjugated matrix could suppress $k_q(\text{RT})$ caused by endothermic triplet–triplet energy transfer from guest to host molecules and effectively protect triplet excited species from oxygen, contributing substantially to the appearance of persistent RTP. Quantum chemical calculations of such rigid hosts also revealed that $k_{nr}(\text{RT})$ based on free intramolecular vibrations is intrinsically small and approaches a very small k_p .^[56] However, for most heavy atom-free conjugated molecular crystals with persistent RTP,^[9,14–16,25,26,46–51] the quantum yield of persistent RTP ($\Phi_p(\text{RT})$) of conjugated molecular crystals with an RTP lifetime approaching to 1 s is often a few percent or less.^[57,58] Small $k_{nr}(\text{RT})$ caused by the suppression of intramolecular vibrations of target chromophores by the strong intermolecular interactions in the crystalline packing has often been considered as a candidate for the origin of the appearance of persistent RTP. However, very recently, cooperative analysis using microscopy and quantum chemical calculations indicated that suppressed triplet diffusion caused by the weak interaction of the molecular orbitals (MOs) related to the transition from T_1 to the ground state (S_0) greatly decreases $k_q(\text{RT})$ is the main cause of the appearance of persistent RTP.^[59] This indicates that the large decrease of $k_q(\text{RT})$ contributes to the weak persistent RTP while the small $\Phi_p(\text{RT})$ of most aromatic crystals with persistent RTP characteristics is intrinsically because $k_p < k_{nr}(\text{RT})$. Therefore, a way to increase k_p without increasing $k_{nr}(\text{RT})$ is crucial to obtain much larger $\Phi_p(\text{RT})$. However, an overall discussion of k_p , $k_{nr}(\text{RT})$, and $k_q(\text{RT})$ and an approach to increase k_p independent of $k_{nr}(\text{RT})$ in conjugated molecular crystals have not been reported as yet.

Here we investigate the electronic structures controlling k_p , $k_{nr}(\text{RT})$, and $k_q(\text{RT})$ of nonpolar and highly symmetric conjugated molecular crystals showing persistent blue-green RTP in air. $\text{C}(\text{C}_6\text{H}_5)_4$, $\text{Si}(\text{C}_6\text{H}_5)_4$, and $\text{Ge}(\text{C}_6\text{H}_5)_4$ as the steric and highly symmetric aromatic structures do not show RTP in degassed solution, whereas they show persistent RTP under ambient conditions in the crystalline state.^[9] The RTP lifetimes ($\tau_p(\text{RT})$) of $\text{C}(\text{C}_6\text{H}_5)_4$, $\text{Si}(\text{C}_6\text{H}_5)_4$, and $\text{Ge}(\text{C}_6\text{H}_5)_4$ crystals in air are 1.10, 1.26, and 0.46 s, respectively. $\Phi_p(\text{RT})$ of $\text{C}(\text{C}_6\text{H}_5)_4$, $\text{Si}(\text{C}_6\text{H}_5)_4$, and $\text{Ge}(\text{C}_6\text{H}_5)_4$ crystals are 3.1%, 5.1%, and 17%, respectively. Analysis of the triplet yields of $\text{C}(\text{C}_6\text{H}_5)_4$, $\text{Si}(\text{C}_6\text{H}_5)_4$, and $\text{Ge}(\text{C}_6\text{H}_5)_4$ in the crystalline state indicates that the appearance of persistent RTP is mostly driven by the large decrease of $k_{nr}(\text{RT}) + k_q(\text{RT})$ caused by crystallization. Analysis using vibrational spin–orbit coupling (VSOC) at RT indicates that the large decrease of $k_{nr}(\text{RT}) + k_q(\text{RT})$ is caused by not the decrease of $k_{nr}(\text{RT})$ but the large decrease of $k_q(\text{RT})$ owing to the small diffusion of triplet excitons at RT. Quantum chemical calculations reveal that the small diffusion of triplet excitons is caused by the small overlap between the highest occupied molecular orbitals (HOMOs), which originates from the localization of the HOMOs over the two phenylene rings induced by the π degeneracy of the steric and highly symmetric conjugated structures. For $\text{Ge}(\text{C}_6\text{H}_5)_4$, the HOMO localization in the highly symmetric conjugated structures also induce moderate charge-transfer (CT) character in transitions between high-order singlet excited states (S_m) and S_0 . Stronger spin–orbit coupling (SOC) between the moderate CT characteristics of the S_m – S_0 transitions

and local excited (LE) characteristics of the T_1 – S_0 transition contribute to the large increase of k_p independent of $k_{nr}(\text{RT})$. This knowledge of electronic characteristics, k_p , $k_{nr}(\text{RT})$, and $k_q(\text{RT})$ of conjugated molecular crystals will be important for realizing efficient persistent RTP from conjugated molecular crystals.

2. Results and Discussion

2.1. Emission Characteristics

The chemical structures of $\text{C}(\text{C}_6\text{H}_5)_4$, $\text{Si}(\text{C}_6\text{H}_5)_4$, and $\text{Ge}(\text{C}_6\text{H}_5)_4$ are shown in **Figure 1a**. **Figure 1b** shows the emission behavior of the crystals upon excitation at 280 nm and after ceasing excitation. The crystals exhibited blue emission upon excitation and then blue–green emission remained after ceasing excitation. To discuss the emission characteristics of $\text{C}(\text{C}_6\text{H}_5)_4$, $\text{Si}(\text{C}_6\text{H}_5)_4$, and $\text{Ge}(\text{C}_6\text{H}_5)_4$, their absorption and emission spectra were measured in tetrahydrofuran (THF) and the crystalline state. In THF, the three compounds absorbed light with an energy higher than 300 nm (**Figure 1c**) and emitted ultraviolet fluorescence from 300 to 400 nm (**Figure 1d**). The fluorescence spectrum shifted to slightly higher energy with increasing atomic weight of center atom (X) of $\text{C}(\text{C}_6\text{H}_5)_4$, $\text{Si}(\text{C}_6\text{H}_5)_4$, and $\text{Ge}(\text{C}_6\text{H}_5)_4$ crystals. Time-dependent density functional theory (TDDFT) calculations also showed a small blueshift of the transition from S_0 to the lowest singlet excited state (S_1) with increasing atomic weight of X (**Table S1**, Supporting Information). The fluorescence quantum yields at RT ($\Phi_f(\text{RT})$) of $\text{C}(\text{C}_6\text{H}_5)_4$, $\text{Si}(\text{C}_6\text{H}_5)_4$, and $\text{Ge}(\text{C}_6\text{H}_5)_4$ in THF were 31%, 18%, and 2.7%, respectively. Because the fluorescence lifetimes at RT ($\tau_f(\text{RT})$) of $\text{C}(\text{C}_6\text{H}_5)_4$, $\text{Si}(\text{C}_6\text{H}_5)_4$, and $\text{Ge}(\text{C}_6\text{H}_5)_4$ were 4.0, 4.4, and 2.7 ns, respectively, the rate constants of fluorescence (k_f) of $\text{C}(\text{C}_6\text{H}_5)_4$, $\text{Si}(\text{C}_6\text{H}_5)_4$, and $\text{Ge}(\text{C}_6\text{H}_5)_4$ determined using $k_f = \Phi_f(\text{RT})/\tau_f(\text{RT})$ were 7.7×10^7 , 4.0×10^7 , and $9.9 \times 10^6 \text{ s}^{-1}$, respectively.

Figure 1e shows the emission spectra of $\text{C}(\text{C}_6\text{H}_5)_4$, $\text{Si}(\text{C}_6\text{H}_5)_4$, and $\text{Ge}(\text{C}_6\text{H}_5)_4$ crystals upon excitation at 280 nm in air. $\text{C}(\text{C}_6\text{H}_5)_4$ and $\text{Si}(\text{C}_6\text{H}_5)_4$ crystals showed distinct emission from 290 to 400 nm, whereas $\text{Ge}(\text{C}_6\text{H}_5)_4$ exhibited a very weak emission peak in this wavelength range along with a tail from the scattering of the excitation light at 280 nm. The emission from 290 to 400 nm was designated as fluorescence because of its decay lifetime of several nanoseconds. The k_f values of $\text{C}(\text{C}_6\text{H}_5)_4$, $\text{Si}(\text{C}_6\text{H}_5)_4$, and $\text{Ge}(\text{C}_6\text{H}_5)_4$ crystals determined from $\Phi_f(\text{RT})$ and $\tau_f(\text{RT})$ were 7.3×10^7 , 2.3×10^7 , and $8.8 \times 10^6 \text{ s}^{-1}$, respectively, which were similar rates to those observed for isolated $\text{C}(\text{C}_6\text{H}_5)_4$, $\text{Si}(\text{C}_6\text{H}_5)_4$, and $\text{Ge}(\text{C}_6\text{H}_5)_4$ molecules in THF. The fluorescence spectrum of the crystals shifted to slightly higher energy with increasing atomic weight of X and TDDFT calculations also showed this tendency (**Table S2**, Supporting Information). The similar fluorescence energy, fluorescence spectral shape, and k_f before and after crystallization suggest that the MOs related to fluorescence of the three compounds did not interact strongly between molecules in the crystalline structures. In addition, this indicates that the transition dipoles related to the S_1 – S_0 transition of each aromatic molecule did not interact strongly in the crystalline structure.

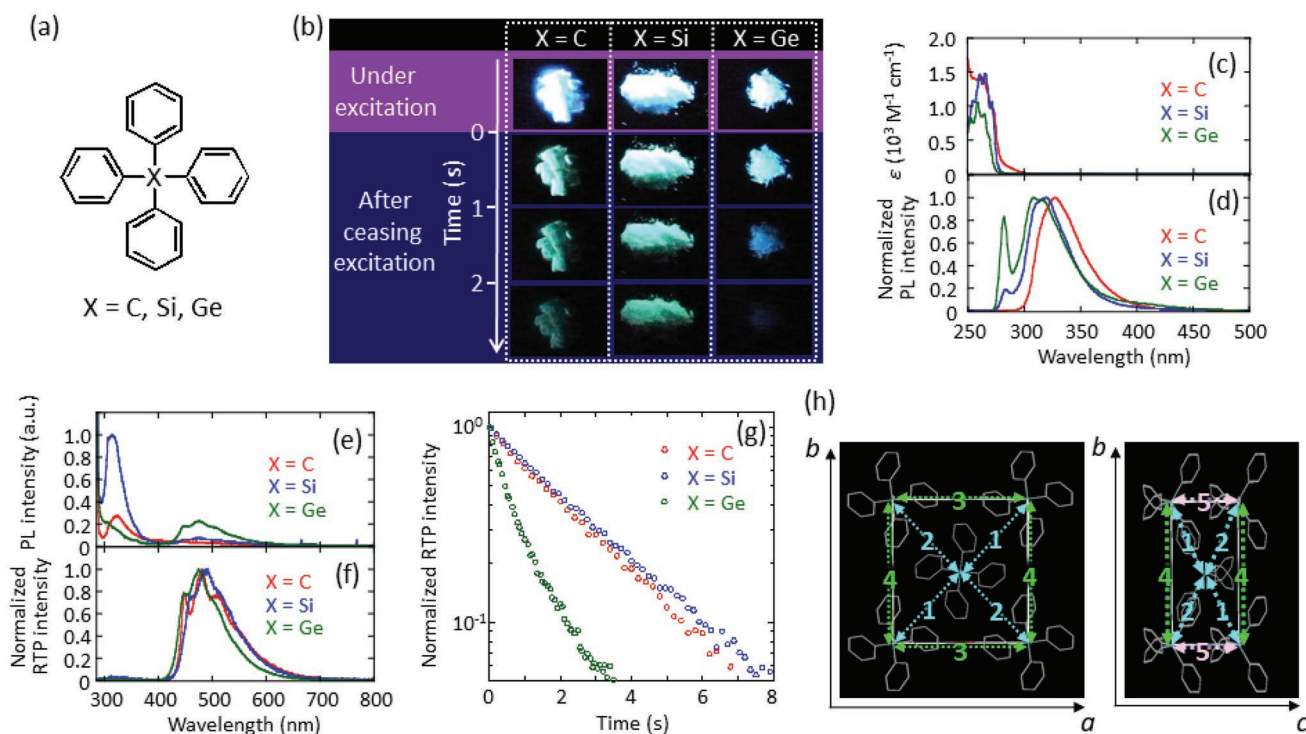


Figure 1. Optical characteristics and crystalline structures of $C(C_6H_5)_4$, $Si(C_6H_5)_4$, and $Ge(C_6H_5)_4$. a) Chemical structures of $C(C_6H_5)_4$, $Si(C_6H_5)_4$, and $Ge(C_6H_5)_4$. b) Changes in the luminescence of the three crystals under excitation at 280 nm and after ceasing excitation. c) Absorption and d) fluorescence spectra in THF at RT. In (d), the peak at 280 nm is caused by scattering of excitation light and the emission intensity was normalized to 1. Emission spectra of the crystals e) under excitation at 280 nm at RT and f) after ceasing excitation. In (e), the rapid increase below 300 nm is caused by scattering of the excitation light from the crystals. In (f), emission intensity was normalized to 1. g) RT emission decay characteristics of the crystals at 490 nm after ceasing excitation. h) Crystalline structures of $Ge(C_6H_5)_4$ at RT.

A large difference between the isolated aromatics in solution and aromatic crystals is the appearance of RTP. Figure 1c also shows that a small emission peak appeared from 400 to 700 nm under excitation at 280 nm. This emission peak was assigned to RTP because it remained for a long time after the excitation was ceased, as reported by Clapp.^[9] Figure 1f shows normalized RTP spectra of the crystals after ceasing excitation at 280 nm. The spectral shape of the emission from the three crystals was comparable with that of the phosphorescence spectra of isolated $C(C_6H_5)_4$, $Si(C_6H_5)_4$, and $Ge(C_6H_5)_4$ in 2-methyl THF frozen at 77 K (Figure S1, Supporting Information). Similar RTP or T_1 energies for the three isolated molecules as well as those of the crystals were also calculated by TD-DFT (Table S1 and S2, Supporting Information). The average $\tau_p(\text{RT})$ values determined for the $C(C_6H_5)_4$, $Si(C_6H_5)_4$, and $Ge(C_6H_5)_4$ crystals in air were 1.10, 1.26, and 0.45 s, respectively (Figure 1g). $\Phi_p(\text{RT})$ of the $C(C_6H_5)_4$, $Si(C_6H_5)_4$, and $Ge(C_6H_5)_4$ crystals in air were 3.1%, 5.1%, and 17%, respectively. We carefully measured $\Phi_p(\text{RT})$ and $\tau_p(\text{RT})$ because triplet accumulation by strong excitation intensity triggers fluorescence resonance energy transfer from S_1 to accumulated triplet excitons, phosphorescence resonance energy transfer from T_1 to accumulated triplet excitons, and triplet-triplet annihilation, which cause underestimation of $\Phi_p(\text{RT})$ and $\tau_p(\text{RT})$.^[12,60,61] We confirmed that underestimation did not occur when 280 nm excitation light with a power of 1.0 mW cm^{-2} was used because linear increases of fluorescence and RTP

were observed around this excitation intensity (Figure S2, Supporting Information). Although there are a few heavy atom-free conjugated crystals with $\Phi_p(\text{RT}) > 10\%$, we note that $\Phi_p(\text{RT})$ of $C(C_6H_5)_4$ and $Si(C_6H_5)_4$ were comparable with those of the recently reported crystallization-induced persistent RTP materials and $\Phi_p(\text{RT})$ of the $Ge(C_6H_5)_4$ crystals was much higher than those of many other conjugated molecular crystals with $\tau_p(\text{RT})$ of $\approx 0.5 \text{ s}$.^[57,58]

2.2. Physical Parameters to Investigate the Generation and Deactivation of Triplet Excitons

To understand the difference of $\Phi_p(\text{RT})$ for the three crystals, intrinsic physical parameters relating RTP can be determined using the quantum yield of phosphorescence at temperature T ($\Phi_p(T)$) and the phosphorescence lifetime at T ($\tau_p(T)$) as shown in the following equations^[12,58,62]

$$\Phi_p(T) = \Phi_{\text{isc}}(T)k_p / (k_p + k_{\text{nr}}(T) + k_q(T)) \quad (1)$$

$$\tau_p(T) = 1 / (k_p + k_{\text{nr}}(T) + k_q(T)) \quad (2)$$

where $\Phi_{\text{isc}}(T)$ is the quantum yield of the triplet yield at T and $k_q(T)$ is the quenching rate caused by oxygen and quenching at T K because of trap states and surface traps after triplet exciton migration. To intrinsically investigate the origin of the

appearance of persistent RTP, the determination of $\Phi_{\text{isc}}(\text{RT})$, k_{p} , $k_{\text{nr}}(\text{RT})$, and $k_{\text{q}}(\text{RT})$ is necessary. However, previous discussions of $\Phi_{\text{isc}}(\text{RT})$, k_{p} , $k_{\text{nr}}(\text{RT})$, and $k_{\text{q}}(\text{RT})$ of heavy atom-free molecules contained numerous assumptions and were phenomenological for the persistent RTP of molecular aggregates. Therefore, a photophysical platform to determine and interpret $\Phi_{\text{isc}}(\text{RT})$, k_{p} , $k_{\text{nr}}(\text{RT})$, and $k_{\text{q}}(\text{RT})$ of heavy atom-free molecular aggregates is crucial for researchers to design state-of-the-art molecular functions for the ultralong-lived RT triplet excitons generated by a variety of heavy-atom free conjugated structures.

2.3. Investigation of $\Phi_{\text{isc}}(\text{RT})$ by Comparison of Experimentally Observed and Theoretical k_{p}

To investigate the origin of the appearance of the RTP characteristics in the crystals, $\Phi_{\text{isc}}(\text{RT})$ of the three types of crystals was estimated. Although $\Phi_{\text{isc}}(\text{RT})$ may often be different between dispersed conjugated molecules and an aggregate of the same molecules because of the change of k_{f} and the rate constant of intersystem crossing (ISC) between S_1 and T_1 at RT ($k_{\text{isc}}(\text{RT})$), no experimental methods to quantify $\Phi_{\text{isc}}(\text{RT})$ of crystalline materials have yet been developed. In this paper, we estimated $\Phi_{\text{isc}}(\text{RT})$ by assuming $\Phi_{\text{isc}}(\text{RT}) \approx 1 - \Phi_{\text{f}}(\text{RT})$.^[18] It is considered that this approximation is generally applicable when there is no conical intersection between S_0 and S_1 in addition to a large energy gap (>2.17 eV) between S_1 and S_0 in the structure after relaxation from the Franck–Condon excited state. $\Phi_{\text{isc}}(\text{RT})$ of $\text{C}(\text{C}_6\text{H}_5)_4$, $\text{Si}(\text{C}_6\text{H}_5)_4$, and $\text{Ge}(\text{C}_6\text{H}_5)_4$ crystals estimated based on $\Phi_{\text{isc}}(\text{RT}) \approx 1 - \Phi_{\text{f}}(\text{RT})$ were 95%, 81%, and 97%, respectively. Then, $\Phi_{\text{isc}}(\text{RT})$, $\Phi_{\text{p}}(\text{RT})$, and $\tau_{\text{p}}(\text{RT})$ were substituted into Equation (3) to determine k_{p}

$$\Phi_{\text{p}}(\text{RT}) = \Phi_{\text{isc}}(\text{RT}) k_{\text{p}} \tau_{\text{p}}(\text{RT}) \quad (3)$$

The calculated k_{p} values of $\text{C}(\text{C}_6\text{H}_5)_4$, $\text{Si}(\text{C}_6\text{H}_5)_4$, and $\text{Ge}(\text{C}_6\text{H}_5)_4$ were 3.0×10^{-2} , 5.0×10^{-2} , and $3.9 \times 10^{-1} \text{ s}^{-1}$, respectively.

To check the validity of the estimated k_{p} values based on $\Phi_{\text{isc}}(\text{RT}) \approx 1 - \Phi_{\text{f}}(\text{RT})$, the experimentally determined k_{p} were compared with k_{p} obtained by quantum chemical calculations. Recently, k_{p} of dispersed heavy atom-free conjugated structures in a highly rigid amorphous matrix was predicted well by TDDFT with SOC which can be included as a perturbation based on the scalar relativistic orbitals (pSOC-TDDFT).^[56] Therefore, the same method was used to calculate k_{p} of the three crystals. X-ray diffraction (XRD) analysis revealed that the three crystals possessed body-centered tetragonal lattices with five kinds of dimers (dimer 1, dimer 2, dimer 3, dimer 4, and dimer 5) in each crystalline structure at RT, as shown in Figure 1h. When the triplet energies of the monomer and dimer 1–5 were calculated without changing the conformation determined by XRD analysis at RT, each of dimer 1–5 had eight triplet states of comparable energy with that of T_1 and other triplet states that were much higher in energy than T_1 (Table S3, Supporting Information). When an i -order triplet state with different energy contained in dimer 1–5 is defined as T_i , dimer 1–5 have 40 triplet states with comparable energy. Because each crystalline lattice of the $\text{C}(\text{C}_6\text{H}_5)_4$, $\text{Si}(\text{C}_6\text{H}_5)_4$, and

$\text{Ge}(\text{C}_6\text{H}_5)_4$ crystals contains the same number of dimer 1–5, k_{p} can be calculated as the average value based on Boltzmann distribution of T_i – S_0 transitions ($i = 1$ –40) using Equation (4)^[63]

$$k_{\text{p}} = \left[\sum_i k_{\text{pi}} \exp(-\Delta E_{T_i-T_1}/kT) \right] / \sum_i \exp(-\Delta E_{T_i-T_1}/kT) \quad (4)$$

where $\Delta E_{T_i-T_1}$ is the energy difference between T_1 and T_i , and k_{pi} is the rate constant of phosphorescence from T_i to S_0 , which was determined by a quantum chemical calculation. In the quantum chemical calculation, configurations confirmed using XRD at RT were used to calculate physical parameters. To calculate k_{p} of the dimers, the SOC operator within the zeroth-order regular approximation was used as the operator for SOC (\bar{H}_{SO}) and k_{p} was treated as a perturbation based on the scalar relativistic orbitals. Hybrid-B3LYP and TZP were used as exchange-correlation functionals and the Slater-type all-electron basis set, respectively. k_{p} of $\text{C}(\text{C}_6\text{H}_5)_4$, $\text{Si}(\text{C}_6\text{H}_5)_4$, and $\text{Ge}(\text{C}_6\text{H}_5)_4$ calculated from Equation (4) using the configurations of dimer 1–5 were 4.7×10^{-2} , 6.4×10^{-2} , and $4.5 \times 10^{-1} \text{ s}^{-1}$, respectively. The calculated k_{p} values are comparable with the experimentally estimated ones assuming $\Phi_{\text{isc}}(\text{RT}) \approx 1 - \Phi_{\text{f}}(\text{RT})$ (Table 1). Therefore, $\Phi_{\text{isc}}(\text{RT}) \approx 1 - \Phi_{\text{f}}(\text{RT})$ is applicable to the three types of crystals and $\text{C}(\text{C}_6\text{H}_5)_4$, $\text{Si}(\text{C}_6\text{H}_5)_4$, and $\text{Ge}(\text{C}_6\text{H}_5)_4$ crystals are considered to display large $\Phi_{\text{isc}}(\text{RT})$. Although we calculated k_{p} using the monomer structures of $\text{C}(\text{C}_6\text{H}_5)_4$, $\text{Si}(\text{C}_6\text{H}_5)_4$, and $\text{Ge}(\text{C}_6\text{H}_5)_4$, the values were overestimated (Table 1). This suggests that T_1 is delocalized in dimers in the crystals. Quantum chemical calculations of the rate constant of ISC from S_1 to T_1 suggested that the very large $\Phi_{\text{isc}}(\text{RT})$ is not caused by crystallization-induced enhancement of $\Phi_{\text{isc}}(\text{RT})$ (Figure S3, Supporting Information). Because $\Phi_{\text{isc}}(\text{RT})$ approaches 100% for the three types of crystals, analysis of all of k_{p} , $k_{\text{nr}}(\text{RT})$, and $k_{\text{q}}(\text{RT})$ is important to understand the origin of persistent RTP from these crystals under ambient conditions.

2.4. Investigation of the Origin of the Small $k_{\text{q}}(\text{RT})$ Including Separation of $k_{\text{nr}}(\text{RT})$ and $k_{\text{q}}(\text{RT})$

To discuss $k_{\text{nr}}(\text{RT})$ and $k_{\text{q}}(\text{RT})$ of the crystals, the temperature dependence of $\tau_{\text{p}}(T)$ was measured, as shown in Figure 2a. $\tau_{\text{p}}(T)$ of $\text{C}(\text{C}_6\text{H}_5)_4$, $\text{Si}(\text{C}_6\text{H}_5)_4$, and $\text{Ge}(\text{C}_6\text{H}_5)_4$ crystals hardly decreased from 77 K to RT. By substituting experimentally determined k_{p} (Table 1) into Equation (2), the Arrhenius plots of $k_{\text{nr}}(T) + k_{\text{q}}(T)$ for the crystals were constructed, as presented in Figure 2b. Each curve could be fitted using a sum of two exponential functions. The increase of $k_{\text{nr}}(T) + k_{\text{q}}(T)$ at higher temperature has been ascribed to the increase of $k_{\text{q}}(T)$, which is caused by quenching of triplet excitons at defects after triplet exciton migration.^[59] The activation energy of triplet exciton migration is theoretically expressed as the sum of the reorganization energies of hole and electron transfer.^[64] The reorganizations induced by hole and electron transfer have large configuration changes compared with those caused by atomic vibrations in a molecule and large reorganizations typically have high activation energies. Therefore, the larger increase of $k_{\text{nr}}(T) + k_{\text{q}}(T)$ at higher temperature in Figure 2b was caused by the increase of $k_{\text{q}}(T)$ triggered by triplet exciton migration and the smaller increase of $k_{\text{nr}}(T) + k_{\text{q}}(T)$ at lower temperature was caused by the increase of $k_{\text{nr}}(T)$ depending on the intramolecular

Table 1. Photophysical parameters of C(C₆H₅)₄, Si(C₆H₅)₄, and Ge(C₆H₅)₄.

Compound	Solution		Solid								
	Exp. ^{a)}	Calc.	Exp.			Calc.			Calc.		
	k_f [s ⁻¹]	$k_p^{b,c)}$ [s ⁻¹]	Φ_f [RT] [%]	k_f [s ⁻¹]	Φ_p [RT] [%]	τ_p [RT] [s]	$k_p^{d)}$ [s ⁻¹]	k_{nr} [RT] ^{d)} [s ⁻¹]	k_q [RT] ^{d)} [s ⁻¹]	$k_p^{b,e)}$ [s ⁻¹]	VSOC[RT] ^{b,f)} [a.u.]
C(C ₆ H ₅) ₄ ^{g)}	7.7×10^7	8.9×10^{-2}	5.1	7.3×10^7	3.1	1.10	3.0×10^{-2}	5.0×10^{-1}	3.6×10^{-1}	4.7×10^{-2}	–
Si(C ₆ H ₅) ₄ ^{g)}	4.0×10^7	1.3×10^{-1}	18.6	2.3×10^7	5.1	1.26	5.0×10^{-2}	5.2×10^{-1}	2.6×10^{-1}	6.4×10^{-2}	4.7×10^2
Ge(C ₆ H ₅) ₄ ^{g)}	9.9×10^6	9.6×10^{-1}	2.8	8.8×10^6	17.0	0.45	3.9×10^{-1}	1.6×10^0	3.5×10^{-1}	4.5×10^{-1}	9.0×10^2
Chrysenes ^{h)}	–	3.5×10^{-3}	16.0	–	0.91	1.36	8.0×10^{-3}	5.7×10^{-1}	1.6×10^{-1}	–	1.0×10^2

^{a)}In THF solution; ^{b)}Information about SOC was treated as a perturbation based on the scalar relativistic orbitals. Hybrid-B3LYP and TZP were used as exchange-correlation functionals and the Slater-type all-electron basis set, respectively; ^{c)}Calculated using monomer structure; ^{d)}Calculated using τ_p (RT) and Φ_{isc} (RT) = 1 – Φ_f (RT); ^{e)}Calculated as average value of dimers 1–5 determined by XRD; ^{f)}VSOC(RT) means P_p (RT) $\langle \partial \langle \Psi_0^{(0)} | \hat{H}_{SO} | \Psi_1^{(0)} \rangle \rangle / \partial Q_p \rangle^2$. Conformations including vibration modes of monomer were optimized at T₁ using density functional theory (Gaussian09/B3LYP/6-31G(d)); ^{g)}Data for solids were measured in the crystalline state; ^{h)}Data for solids were measured for 0.3 wt% chrysenes-doped β -estradiol in the amorphous state.

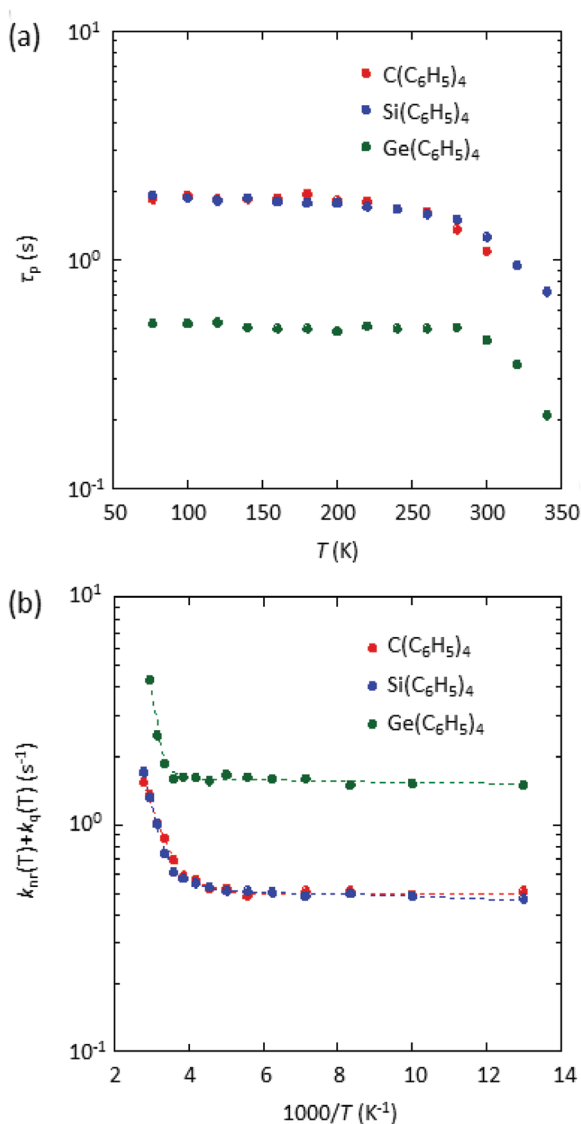


Figure 2. Temperature dependence of the phosphorescence characteristics of C(C₆H₅)₄, Si(C₆H₅)₄, and Ge(C₆H₅)₄ crystals. a) τ_p (T). b) $k_{nr}(T) + k_q(T)$. Dashed lines are fitted with a sum of two exponential functions.

vibrations of chromophores.^[12,56,58,59,65,66] By using an exponential function at higher temperature for each crystal, k_q (RT) of C(C₆H₅)₄, Si(C₆H₅)₄, and Ge(C₆H₅)₄ crystals were quantified as 3.6×10^{-1} , 2.6×10^{-1} , and 3.5×10^{-1} s⁻¹, respectively. Thus, very small and comparable quenching of triplet excitons at RT was observed for the three crystals.

Recently, indeed cooperative analysis of the diffusion length of triplet excitons at RT (L_T (RT)) using a microscopic technique and estimation of L_T (RT) using a quantum chemical calculation verified that k_q (RT) observed at higher temperature was mainly affected by quenching of triplet excitons at trap sites after triplet exciton migration.^[59] In this analysis, it was considered that k_q (RT) was proportional to the diffusion constant of triplet excitons at RT (D_T (RT)) when crystals had comparable defect densities for triplet excitons. D_T (RT) is generally expressed as

$$D_T(\text{RT}) = L_T(\text{RT})^2 / \tau_p(\text{RT}) \quad (5)$$

To experimentally obtain L_T (RT), a 2D RTP pattern can be compared with the 2D pattern of excitation light obtained when the excitation light is focused on a single crystal.^[59] However, the analysis of C(C₆H₅)₄, Si(C₆H₅)₄, and Ge(C₆H₅)₄ single crystals requires high-resolution focusing of excitation light below 320 nm using an objective lens with large numerical aperture (NA); such light is not able to penetrate commercially available objective lenses. Although excitation by two-photon absorption using nanosecond laser pulses at 355 nm was attempted, no persistent RTP signal was obtained from C(C₆H₅)₄, Si(C₆H₅)₄, and Ge(C₆H₅)₄ crystals. In the previous approach, however, D_T (RT) was well estimated from the transfer integrals of holes and electrons related to triplet excitons by quantum chemical calculations using crystalline structures. D_T (RT) can be expressed based on the concept of double charge transfer as follows^[64]

$$D_T(\text{RT}) \propto H_e^2 H_h^2 \quad (6)$$

where H_e is the transfer integral of lowest unoccupied molecular orbitals (LUMOs) and H_h is the transfer integral of HOMOs. Therefore, $H_e^2 H_h^2$ of C(C₆H₅)₄, Si(C₆H₅)₄, and Ge(C₆H₅)₄ crystals was investigated. Because the $H_e^2 H_h^2$ value

of dimer 5 shown in Figure 1h was much larger than those of dimer 1–4 for Si(C₆H₅)₄ and Ge(C₆H₅)₄ crystals (Table S4, Supporting Information), the $H_e^2H_h^2$ value of dimer 5 is important to discuss triplet exciton diffusion in Si(C₆H₅)₄ and Ge(C₆H₅)₄ crystals. For the C(C₆H₅)₄ crystal, dimer 2 had the largest value of $H_e^2H_h^2$. The highest $H_e^2H_h^2$ values for C(C₆H₅)₄, Si(C₆H₅)₄, and Ge(C₆H₅)₄ crystals were 1.1×10^{-8} , 1.7×10^{-7} , and 7.5×10^{-8} eV⁴, respectively (Figure 3a). In our previous report, 9-(3,5-dichlorophenyl)-9H-carbazole (CzDCIT) crystals with τ_p (RT) of 0.61 s exhibited very small D_T (RT) (3×10^{-9} cm² s⁻¹) and L_T (RT) (<0.42 μ m), as shown in Figure 3a.^[59] This report showed that the largest $H_e^2H_h^2$ value of a dimer along the *b*-axis of CzDCIT crystals was 6.3×10^{-8} eV⁴ (Figure 3a). That is, CzDCIT, C(C₆H₅)₄, Si(C₆H₅)₄, and Ge(C₆H₅)₄ crystals have comparable $H_e^2H_h^2$. Therefore, it could be considered that C(C₆H₅)₄, Si(C₆H₅)₄, and Ge(C₆H₅)₄ crystals have very small L_T (RT), similar to CzDCIT crystals, and the inefficient migration of triplet excitons in the three crystals results in the minimization of k_q (RT).

For C(C₆H₅)₄, Si(C₆H₅)₄, and Ge(C₆H₅)₄ crystals, it might be generally considered that the small D_T (RT) is caused by the

large twisted aromatic structures. However, we note that $|H_e|$ of dimer 5 of Si(C₆H₅)₄ and Ge(C₆H₅)₄ are comparable to that of dimers in a rubrene single crystal (4.7×10^{-2} eV), which has very large D_T (RT) (Figure 3a).^[67] Compared with the large $|H_e|$, dimer 5 of Si(C₆H₅)₄ and Ge(C₆H₅)₄ have much smaller $|H_h|$. Therefore, small overlap between the HOMOs of the monomers in dimer 5 causes the small L_T (RT) and results in the small k_q (RT) below 10^0 s⁻¹. Figure 3b presents the relationship between the HOMOs of the two monomers (monomer 1 and 2) in dimer 5 of a Ge(C₆H₅)₄ crystal. Each monomer had two comparable MOs corresponding to HOMOs ((i) of Figure 3b). Interestingly, the HOMOs of both monomer 1 and 2 were not delocalized over all four phenylene rings but were instead localized over two phenylene rings. The localization of a HOMO over only two phenylene rings was caused by the degeneracy of the highly symmetric four-phenylene rings of C(C₆H₅)₄, Si(C₆H₅)₄, and Ge(C₆H₅)₄ structure.^[68] Because the two monomers were located such that the overlap of their HOMOs was minimized ((ii) of Figure 3b), HOMOs with very small splitting energy, approximately corresponding to $2|H_h|$, were obtained. Small $|H_h|$ based on the same mechanism were also determined for

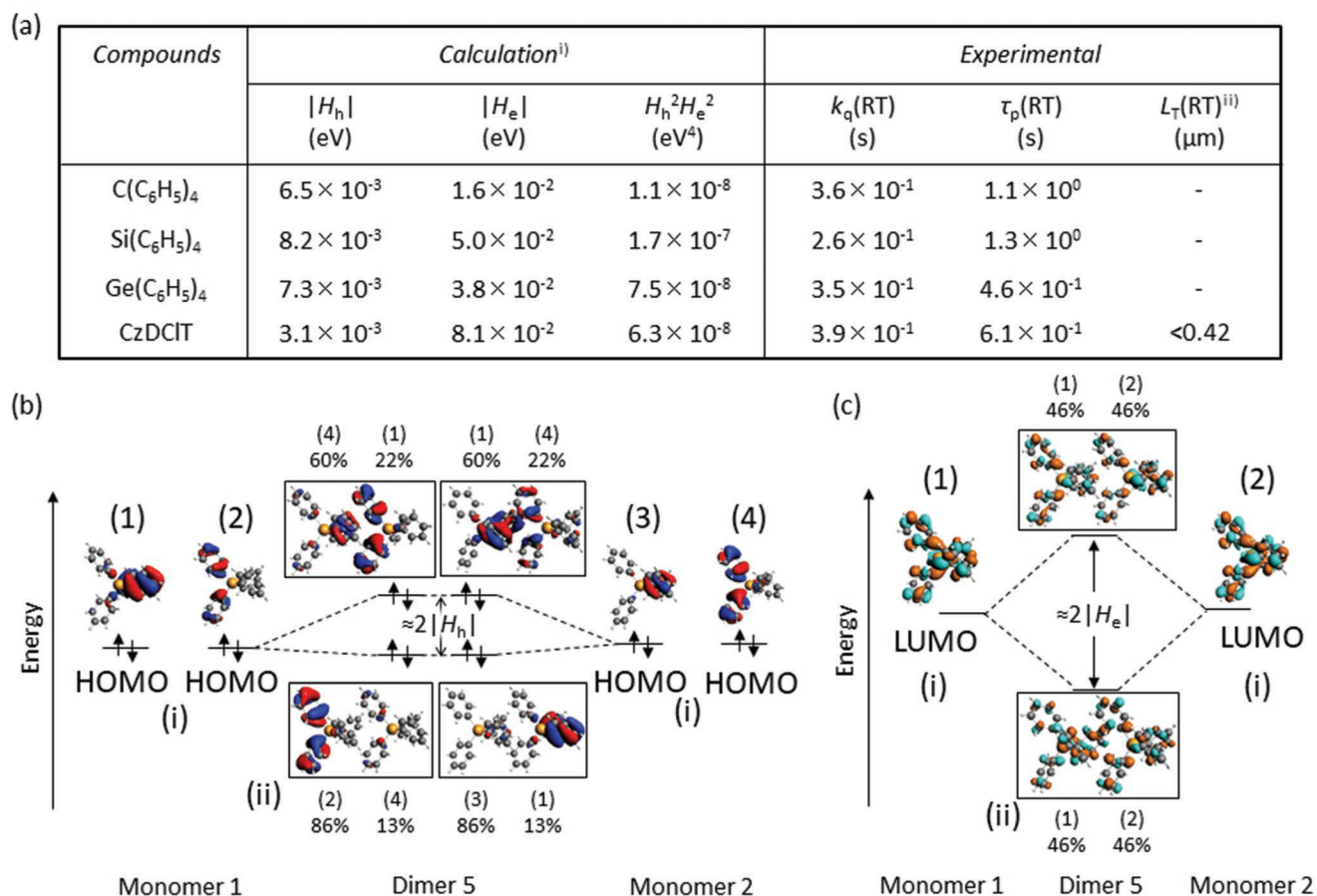


Figure 3. Comparison of calculated physical parameters related to diffusion of triplet excitons and illustration of the difference of hole and electron transfer integrals using molecular orbitals. a) Summary of $|H_h|$ and $|H_e|$ of a representative dimer showing the largest $H_h^2H_e^2$ and experimentally observed k_q (RT), τ_p (RT), and L_T (RT) in air of C(C₆H₅)₄, Si(C₆H₅)₄, and Ge(C₆H₅)₄. i) Conformations in crystalline structures determined by XRD are used. GGA:PW91 and TZP were used as exchange-correlation functionals and the Slater-type all-electron basis, respectively, to calculate $|H_h|$ and $|H_e|$. Data of dimer 3 for C(C₆H₅)₄. Data of dimer 5 for Si(C₆H₅)₄ and Ge(C₆H₅)₄. ii) The value is determined using microscope in ref. [59]. b) Structures of molecular orbitals causing the small $|H_h|$ of dimer 5 in the Ge(C₆H₅)₄ crystalline lattice. c) Structures of molecular orbitals related to the large $|H_e|$ of dimer 5 in the Ge(C₆H₅)₄ crystalline lattice.

the Si(C₆H₅)₄ and C(C₆H₅)₄ crystals (Figure S4a,b, Supporting Information). For electron transfer, the LUMOs of monomer 1 and 2 were delocalized over all four phenylene rings ((i) in Figure 3c). Consequently, the large overlap of the LUMOs leads to large |H_e|, as visually observed for dimer 5 of a Ge(C₆H₅)₄ crystal ((ii) in Figure 3c) and Si(C₆H₅)₄ and C(C₆H₅)₄ crystals (Figure S4c,d, Supporting Information respectively). Although the MOs of a triphenylsilane molecule as an asymmetric structure were checked, its HOMO and LUMO were both delocalized over the whole molecule because of the lack of π degeneracy, causing large overlap of HOMOs between molecules, which facilitates triplet exciton migration (Figure S5, Supporting Information). We note that 2D highly symmetric structures often have large overlap of MOs related to triplet exciton diffusion because of the effective stacking of planar conjugated structures, although each monomer has two kinds of moderately separated HOMOs caused by the π degeneracy (Figure S6, Supporting Information). Therefore, steric hindrance and a highly symmetric structure may be important to achieve very small overlap of MOs related to triplet exciton diffusion despite their close molecular packing in crystalline structures. Although the above discussion is based on the assumption that triplet excitons are localized in monomers, in Section 2.2. the estimation of k_p by quantum chemical calculations was more accurate when triplet excitons were delocalized over dimers (Table 1). We note that analysis regarding the transfer integrals between two dimers contained in crystalline structure also indicates that the localization of HOMOs caused by the steric and highly symmetric structures in C(C₆H₅)₄, Si(C₆H₅)₄, and Ge(C₆H₅)₄ triggers inefficient hole transfer (Section 3 and Figure S7 in the Supporting Information), which contributes to the suppressed triplet exciton diffusion and leads to the minimization of k_q(RT).

2.5. Investigation of k_{nr}(RT) for the Three Types of Crystals

The separation of k_q(RT) based on the discussion of the small triplet exciton diffusion length of the C(C₆H₅)₄, Si(C₆H₅)₄, and Ge(C₆H₅)₄ crystals allows us to quantify k_{nr}(RT) of the three types of crystals. The small increase of k_{nr}(T) + k_q(T) from 77 to 260 K is caused by vibration-based nonradiative deactivation from T₁. Using the exponential fitting line at lower temperature in Figure 2b, k_{nr}(RT) of C(C₆H₅)₄, Si(C₆H₅)₄, and Ge(C₆H₅)₄ crystals were quantified as 5.0 × 10⁻¹, 5.2 × 10⁻¹, and 1.6 × 10⁰ s⁻¹, respectively. Thus, k_{nr}(RT) of Ge(C₆H₅)₄ crystals is 3.2 and 3.1 times larger than those of C(C₆H₅)₄ and Si(C₆H₅)₄ crystals, respectively. Using theoretical equations containing a VSOC term explained in the 1970s,^[69,70] k_{nr}(RT) of a variety of dispersed heavy atom-free conjugated molecules have recently been predicted using VSOC considering vibrational factors at RT. In these calculations, dispersed heavy atom-free conjugated molecules with comparable T₁ energy could be approximately predicted using $\Sigma P_p(RT) |\partial \langle \Psi_0^{(0)} | \overline{H}_{SO} | \Psi_1^{(0)} \rangle / \partial Q_p|^2$, where $\Psi_0^{(0)}$ is the wavefunction of S₀ with normal vibrations, $\Psi_1^{(0)}$ is the wavefunction of T₁ with normal vibrations, H_{SO} is the Hamiltonian operator related to SOC, P_p(RT) is the vibrational factor at RT, and Q_p is the coordinate of atoms.^[56] Figure 4 illustrates the relationship between $P_p(RT) |\partial \langle \Psi_0^{(0)} | \overline{H}_{SO} | \Psi_1^{(0)} \rangle / \partial Q_p|^2$ and wavenumber

(ω_p) for Si(C₆H₅)₄ and Ge(C₆H₅)₄ crystals. By integrating the signals in Figure 5, $\Sigma P_p(RT) |\partial \langle \Psi_0^{(0)} | \overline{H}_{SO} | \Psi_1^{(0)} \rangle / \partial Q_p|^2$ of Si(C₆H₅)₄ and Ge(C₆H₅)₄ crystals were determined to be 4.7 × 10² and 9.0 × 10² a.u., respectively. We previously reported that nonaggregated chrysene showing green T₁ energy has k_{nr}(RT) of 5 × 10⁻¹ s⁻¹ in rigid short conjugated amorphous media and $\Sigma P_p(RT) |\partial \langle \Psi_0^{(0)} | \overline{H}_{SO} | \Psi_1^{(0)} \rangle / \partial Q_p|^2$ of chrysene was calculated to be 1.0 × 10² a.u. (Table 1).^[56] By considering the ratios of $\Sigma P_p(RT) |\partial \langle \Psi_0^{(0)} | \overline{H}_{SO} | \Psi_1^{(0)} \rangle / \partial Q_p|^2$ for Si(C₆H₅)₄, Ge(C₆H₅)₄, and chrysene as well as k_{nr}(RT) = 5 × 10⁻¹ s⁻¹ for dispersed chrysene, k_{nr}(RT) of Si(C₆H₅)₄ and Ge(C₆H₅)₄ crystals were estimated to increase up to 2.5 × 10⁰ and 4.5 × 10⁰ s⁻¹, respectively, if the molecules freely vibrate in the crystalline structures. However, experimentally observed k_{nr}(RT) of Si(C₆H₅)₄ and Ge(C₆H₅)₄ crystals were less than half of the estimated values. Therefore, some vibrations of Si(C₆H₅)₄ and Ge(C₆H₅)₄ molecules in the crystals are slightly suppressed compared with those of an isolated molecule. The large decrease of the nonradiative deactivation from T₁ after crystallization is often attributed to the restriction of the molecular vibrations of the conjugated molecules in the crystal lattice. However, we note that at least for C(C₆H₅)₄, Si(C₆H₅)₄, and Ge(C₆H₅)₄ crystals, the decrease is mostly caused by the decrease of k_q(RT) and the vibrations of molecules in the crystalline state are not strongly related to the large decrease of nonradiative deactivation from T₁ at RT. Although the emission spectrum becomes very sharp if the vibrations are largely suppressed, the lack of sharp features observed for the C(C₆H₅)₄, Si(C₆H₅)₄, and Ge(C₆H₅)₄ crystals also indicates the weak suppression of molecular vibrations in the crystalline structure. The appearance of persistent RTP from Si(C₆H₅)₄ doped in Zeonex under high vacuum conditions also supports this conclusion (Figure S8, Supporting Information).

The discussion in Section 2.4 and 2.5 indicates that quenching caused by triplet exciton diffusion is the main reason for the accelerated nonradiative deactivation from T₁ at RT for C(C₆H₅)₄, Si(C₆H₅)₄, and Ge(C₆H₅)₄ crystals and molecular vibrations hardly affect triplet deactivation. Therefore, control of electronic structures to minimize triplet exciton migration at RT in dense conjugated molecular packing is a feasible approach to obtain ultralong-lived T₁ at RT to realize persistent RTP characteristics from heavy atom-free conjugated molecular crystals. Although it is unclear if this is the case for all recently reported aromatic crystals, our previous report using a recent representative aromatic crystal with persistent RTP characteristics and this report investigating an old example of nonpolar aromatic crystals with persistent RTP characteristics suggest that this mechanism is applicable to a variety of aromatic crystals.

2.6. Discussion of the Large Difference of k_p between the Three Types of Crystals

The suppression of the migration of triplet excitons at RT contributes to the appearance of ultralong-lived RT triplet excitons of the C(C₆H₅)₄, Si(C₆H₅)₄, and C(C₆H₅)₄ crystals. Meanwhile, k_p > k_{nr}(RT) is necessary to obtain more efficient persistent RTP characteristics. Ge(C₆H₅)₄ crystals show much larger Φ_p(RT) compared with those of Si(C₆H₅)₄ and C(C₆H₅)₄ crystals. Table 1 reveals that k_{nr}(RT) of the Ge(C₆H₅)₄ crystals is 3.1 times

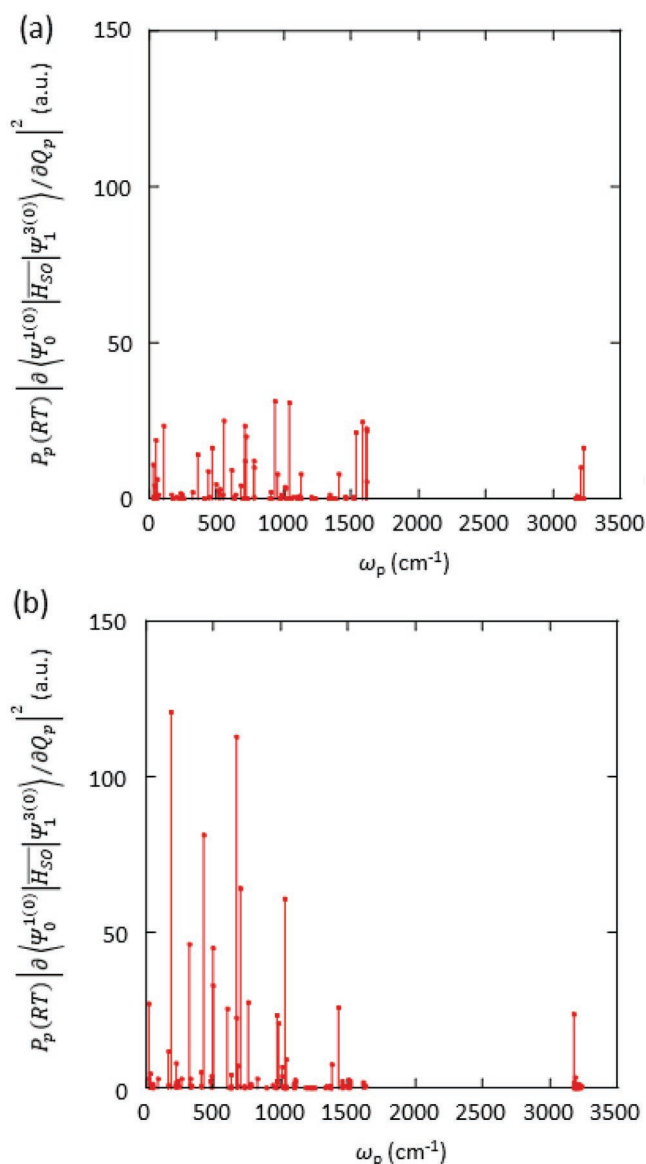


Figure 4. Relationship between $P_p(\text{RT}) \left| \frac{\partial \langle \Psi_0^{(0)} | \overline{H_{SO}} | \Psi_1^{(0)} \rangle}{\partial Q_p} \right|^2$ and ω_p for a) $\text{Si}(\text{C}_6\text{H}_5)_4$ and b) $\text{Ge}(\text{C}_6\text{H}_5)_4$ monomers. Conformations including normal vibration modes were optimized at T_1 using density functional theory (Gaussian09/B3LYP/6-31G(d)). SOC data were treated as perturbations based on the scalar relativistic orbitals. Hybrid-B3LYP and TZP were used as exchange-correlation functionals and the Slater-type all-electron basis set, respectively.

higher than that of the $\text{Si}(\text{C}_6\text{H}_5)_4$ crystals and k_p of $\text{Ge}(\text{C}_6\text{H}_5)_4$ is 7.6 times larger than that of $\text{Si}(\text{C}_6\text{H}_5)_4$. Although this causes the much larger $\Phi_p(\text{RT})$ of $\text{Ge}(\text{C}_6\text{H}_5)_4$ compared with those of the other types of crystals, the reason for the increase of k_p independent of $k_{nr}(\text{RT})$ in conjugated crystalline materials is still unclear for conjugated molecular crystals. To discuss this point, physical factors related to k_p were investigated for the three crystals.

Recently, good predictions of k_p of several dispersed heavy atom-free aromatic structures using pSOC-TDDFT have been reported.^[56] For each dimer 1–5 of $\text{C}(\text{C}_6\text{H}_5)_4$, $\text{Si}(\text{C}_6\text{H}_5)_4$, and

$\text{Ge}(\text{C}_6\text{H}_5)_4$ crystals, k_p was approximated using the following equations^[56,71]

$$k_p \propto \sum_m (\mu_{S_m \rightarrow S_0} \lambda_m)^2 \quad (7)$$

$$\lambda_m \approx \frac{\sum_n \frac{|\langle \Psi_m^1 | \overline{H_{SO}} | \Psi_n^3 \rangle|^2}{|\Delta E_{S_m - T_n}|} \exp\left(-\frac{\Delta E_{T_n - T_1}}{kT}\right)}{\sum_n \exp\left(-\frac{\Delta E_{T_n - T_1}}{kT}\right)}, \quad (n = 1-8) \quad (8)$$

where $\mu_{S_m \rightarrow S_0}$ is the transition dipole moment from S_m to S_0 , Ψ_m^1 is the wavefunction of S_m , Ψ_n^3 is the wavefunction of T_n , $\Delta E_{S_m - T_n}$ is the energy difference between S_m and T_n , and $\Delta E_{T_n - T_1}$ is the energy difference between T_n and T_1 . Again, because each dimer has eight triplet states with comparable energy ($n = 1-8$), λ_m in Equation (8) was considered as the average value for $n = 1-8$. Equations (7) and (8) indicate that large $\mu_{S_m \rightarrow S_0}^2$, large $|\langle \Psi_m^1 | \overline{H_{SO}} | \Psi_n^3 \rangle|^2$, and small $|\Delta E_{S_m - T_n}|^2$ approximately lead to large k_p . Because a large difference was observed between k_p of $\text{Si}(\text{C}_6\text{H}_5)_4$ and $\text{Ge}(\text{C}_6\text{H}_5)_4$ crystals, the following three paragraphs discuss which of $\mu_{S_m \rightarrow S_0}^2$, $|\langle \Psi_m^1 | \overline{H_{SO}} | \Psi_n^3 \rangle|^2$, and $|\Delta E_{S_m - T_n}|^2$ contributes the most to the enhancement of k_p for $\text{Ge}(\text{C}_6\text{H}_5)_4$ crystals.

Moderate CT characteristics of the $S_m - S_0$ transitions and strong LE characteristics of the $T_n - S_0$ transitions ($n = 1-8$) increase $|\langle \Psi_m^1 | \overline{H_{SO}} | \Psi_n^3 \rangle|^2$. Figure 5a displays the relationship between $|\langle \Psi_m^1 | \overline{H_{SO}} | \Psi_n^3 \rangle|^2$ and m of dimer 2 for $\text{C}(\text{C}_6\text{H}_5)_4$, $\text{Si}(\text{C}_6\text{H}_5)_4$, and $\text{Ge}(\text{C}_6\text{H}_5)_4$ crystals. When $|\langle \Psi_9^1 | \overline{H_{SO}} | \Psi_3^3 \rangle|^2$ of $\text{Ge}(\text{C}_6\text{H}_5)_4$ crystals is focused (yellow background of Figure 5a), $|\langle \Psi_9^1 | \overline{H_{SO}} | \Psi_1^3 \rangle|^2$, $|\langle \Psi_9^1 | \overline{H_{SO}} | \Psi_7^3 \rangle|^2$, and $|\langle \Psi_9^1 | \overline{H_{SO}} | \Psi_8^3 \rangle|^2$ are large whereas other $|\langle \Psi_9^1 | \overline{H_{SO}} | \Psi_n^3 \rangle|^2$ are very small. Figure 5b presents MOs related to $|\langle \Psi_9^1 | \overline{H_{SO}} | \Psi_3^3 \rangle|^2$ of dimer 2 of $\text{Ge}(\text{C}_6\text{H}_5)_4$ crystals. In the $S_9 - S_0$ transition, an electron is delocalized over four phenylene rings in S_0 and partly localized over two phenylene rings in S_9 . Therefore, the $S_9 - S_0$ transition has moderate CT character. Thus, moderate CT characteristics are caused by the localization of the HOMOs of dimer 5 over two phenylene rings. The localization of HOMOs in dimer 5 is also caused by the localization of the HOMO of each monomer over two phenylene rings, as explained above (see Figure 3b). Unlike the moderate CT character of the $S_9 - S_0$ transition, the $T_7 - S_0$ transition has multiple LE characteristics. Because SOC between CT and LE characteristics is large according to the El-Sayed rule,^[72] this contributes to the large increase of $|\langle \Psi_9^1 | \overline{H_{SO}} | \Psi_3^3 \rangle|^2$. Figure 5c depicts MOs related to $|\langle \Psi_9^1 | \overline{H_{SO}} | \Psi_4^3 \rangle|^2$ and the $T_4 - S_0$ transition has multiple CT characteristics. The similar CT characteristics of the $S_9 - S_0$ and $T_4 - S_0$ transitions will cause small $|\langle \Psi_9^1 | \overline{H_{SO}} | \Psi_4^3 \rangle|^2$ according to the El-Sayed rule. Checking the character of other transitions revealed that $S_m - S_0$ transitions always have CT character and $T_n - S_0$ transitions ($n = 1-8$) have multiple LE transition characteristics when large $|\langle \Psi_m^1 | \overline{H_{SO}} | \Psi_n^3 \rangle|^2$ is obtained (Figure S9, Supporting Information). Indeed, $|\langle \Psi_m^1 | \overline{H_{SO}} | \Psi_n^3 \rangle|^2$ becomes small when a $S_m - S_0$ transition has CT character and $T_n - S_0$ transition ($n = 1-8$) is mainly composed of multiple CT transitions (Figure S10a–c, Supporting Information). In addition, we noticed that $|\langle \Psi_m^1 | \overline{H_{SO}} | \Psi_n^3 \rangle|^2$ becomes small when an $S_m - S_0$

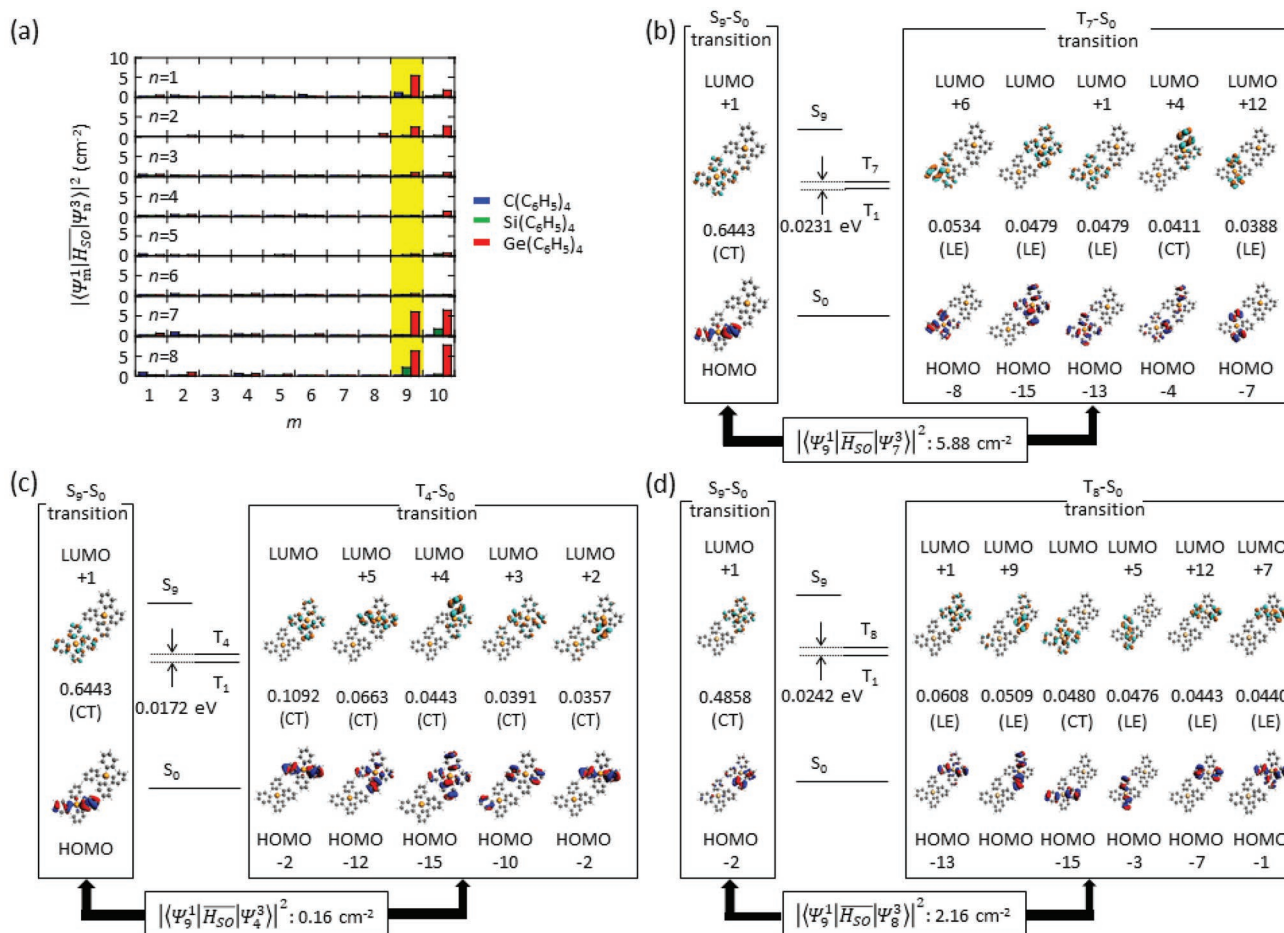


Figure 5. SOC between S_m and T_n ($n = 1-8$) and MOs involved in the SOC of dimer 2 of C(C₆H₅)₄, Si(C₆H₅)₄, and Ge(C₆H₅)₄ crystals. a) Relationship between $\langle \Psi_m^1 | \overline{H}_{SO} | \Psi_n^3 \rangle^2$ and m for dimer 2 of C(C₆H₅)₄, Si(C₆H₅)₄, and Ge(C₆H₅)₄. b) MOs related to the S₉-S₀ and T₇-S₀ transitions of dimer 2 of Ge(C₆H₅)₄. c) MOs related to the S₉-S₀ and T₄-S₀ transitions of dimer 2 of Ge(C₆H₅)₄. d) MOs related to the S₉-S₀ and T₈-S₀ transitions of dimer 2 of Si(C₆H₅)₄.

transition has mixed CT and LE characteristics (Figure S10d, Supporting Information). The mixture of multiple transition characteristics potentially lessens the difference between the characteristics of S_m -S₀ and T_n -S₀ transitions. This tendency was also observed for other dimers of Ge(C₆H₅)₄. Therefore, π degeneracy caused by highly symmetric structure induces moderate CT characteristics in S_m , which contributes to large $\langle \Psi_m^1 | \overline{H}_{SO} | \Psi_n^3 \rangle^2$ and leads to the increase of k_p .

We note that heavy atom effect accelerated k_p but did not contribute to the increase of Φ_p (RT). Figure 5d shows MOs related to $\langle \Psi_m^1 | \overline{H}_{SO} | \Psi_n^3 \rangle^2$ of dimer 2 of Si(C₆H₅)₄. The S₉-S₀ transition has moderate CT character that is similar to the characteristics of the S₉-S₀ transition of dimer 2 of Ge(C₆H₅)₄ crystals. Furthermore, the T₈-S₀ transition of dimer 2 of Si(C₆H₅)₄ contains strong LE characteristics (Figure 5d), which is also similar to the T₇-S₀ transition of dimer 2 of Ge(C₆H₅)₄ crystals (Figure 5b). Therefore, values of SOC are considered to be comparable if the Ge atom of Ge(C₆H₅)₄ does not affect the SOC. However, $\langle \Psi_m^1 | \overline{H}_{SO} | \Psi_n^3 \rangle^2$ of dimer 2 of Ge(C₆H₅)₄ crystals (5.88 cm⁻²) is 2.7 times larger than $\langle \Psi_m^1 | \overline{H}_{SO} | \Psi_n^3 \rangle^2$ of dimer 2 of Si(C₆H₅)₄ crystals (2.16 cm⁻²). Thus, the large positive charge of the Ge nucleus

in $|H_{SO}|$ also partly contributed to the increase of $\langle \Psi_m^1 | \overline{H}_{SO} | \Psi_n^3 \rangle^2$ of the Ge(C₆H₅)₄ crystals. However, the experimentally quantified k_{nr} (RT) of Ge(C₆H₅)₄ crystals was also 3.1 times larger than that of Si(C₆H₅)₄ crystals. The similar values can be reasonably explained by the heavy atom effect increasing k_{nr} (RT) and k_p by the same magnitude. However, the enhancement of k_p of Ge(C₆H₅)₄ crystals compared with that of Si(C₆H₅)₄ crystals is larger than is the case for k_{nr} (RT).

The Ge(C₆H₅)₄ crystal had many moderate CT states at S_m compared with the situations for the Si(C₆H₅)₄ and C(C₆H₅)₄ crystals, which mainly contributed to the increase of Φ_p (RT). The number of S_m - T_n ($n = 1-8$) transitions with $\langle \Psi_m^1 | \overline{H}_{SO} | \Psi_n^3 \rangle^2 > 5.1$ cm⁻² for dimer 2 was counted for the Ge(C₆H₅)₄ crystal. Because the contribution of the heavy atom effect to the increase of $\langle \Psi_m^1 | \overline{H}_{SO} | \Psi_n^3 \rangle^2$ increased by ≈ 3 times upon moving from Si(C₆H₅)₄ to Ge(C₆H₅)₄, the number of S_m - T_n ($n = 1-8$) transitions with $\langle \Psi_m^1 | \overline{H}_{SO} | \Psi_n^3 \rangle^2 > 1.7$ cm⁻², where 1.7 (5.1/3) was used to exclude the contribution of the heavy atom effect to $\langle \Psi_m^1 | \overline{H}_{SO} | \Psi_n^3 \rangle^2$, was determined. Ge(C₆H₅)₄ had five kinds of S_m - T_n transitions with $\langle \Psi_m^1 | \overline{H}_{SO} | \Psi_n^3 \rangle^2 > 5.1$ cm⁻² for dimer 2 whereas dimer 2 of Si(C₆H₅)₄ had only two

kinds of S_m-T_n transitions with $|\langle \Psi_n^1 | \overline{H}_{S_0} | \Psi_n^3 \rangle|^2 > 1.7 \text{ cm}^{-2}$ (Table S5, Supporting Information). This tendency was also observed for other dimers (Tables S6–S8, Supporting Information). Because the increase of $|\langle \Psi_m^1 | \overline{H}_{S_0} | \Psi_n^3 \rangle|^2$ can increase k_p independent of k_{nr} (RT), the formation of many states with moderate CT characteristics in S_m is an origin of the large Φ_p (RT) of $\text{Ge}(\text{C}_6\text{H}_5)_4$.

In Equations (7) and (8), the increase of $|\langle \Psi_m^1 | \overline{H}_{S_0} | \Psi_n^3 \rangle|^2$ mainly contributed to the large enhancement of k_p of $\text{Ge}(\text{C}_6\text{H}_5)_4$ crystals compared with those of $\text{C}(\text{C}_6\text{H}_5)_4$ and $\text{Si}(\text{C}_6\text{H}_5)_4$ crystals, whereas the other two factors ($\mu_{S_m \rightarrow S_0}$ and $|\Delta E_{S_m-T_n}|$) did not contribute to k_p . Figure 6a presents the $\mu_{S_m \rightarrow S_0}$ for dimer 2 of $\text{C}(\text{C}_6\text{H}_5)_4$, $\text{Si}(\text{C}_6\text{H}_5)_4$, and $\text{Ge}(\text{C}_6\text{H}_5)_4$ crystals, which were shown in Table S9 (Supporting Information). The sum of $\mu_{S_m \rightarrow S_0}^2$ for all m ($\sum_m \mu_{S_m \rightarrow S_0}^2$) is proportional to k_p , as shown in Equation (7). Figure 6a indicates $\sum_m \mu_{S_m \rightarrow S_0}^2$ were similar for the three types of crystals because the ratio of $\sum_m \mu_{S_m \rightarrow S_0}^2$ of $\text{C}(\text{C}_6\text{H}_5)_4$, $\text{Si}(\text{C}_6\text{H}_5)_4$, and $\text{Ge}(\text{C}_6\text{H}_5)_4$ crystals was 1.00:1.14:1.26. Therefore, $\mu_{S_m \rightarrow S_0}^2$ hardly contributes to the enhancement of k_p in the $\text{Ge}(\text{C}_6\text{H}_5)_4$ crystals. Figure 6b shows the average of $|\langle \Psi_m^1 | \overline{H}_{S_0} | \Psi_n^3 \rangle|^2$ for n of dimer 2 of $\text{C}(\text{C}_6\text{H}_5)_4$, $\text{Si}(\text{C}_6\text{H}_5)_4$, and $\text{Ge}(\text{C}_6\text{H}_5)_4$ crystals, which were determined using data provided in Table S5 (Supporting Information). The increase of $|\langle \Psi_m^1 | \overline{H}_{S_0} | \Psi_n^3 \rangle|^2$ of $\text{Ge}(\text{C}_6\text{H}_5)_4$ crystals compared with those of $\text{C}(\text{C}_6\text{H}_5)_4$ and $\text{Si}(\text{C}_6\text{H}_5)_4$ crystals in the cases of $m = 9$ and 10 strongly contributed to the enhancement

of k_p of the $\text{Ge}(\text{C}_6\text{H}_5)_4$ crystals. Figure 6c presents the average λ_m^2 for all n of dimer 2, which were calculated using Equation (8). The shape of the distribution of the dependence of λ_m^2 on m (Figure 6c) was similar to that of $|\langle \Psi_m^1 | \overline{H}_{S_0} | \Psi_n^3 \rangle|^2$ on m (Figure 6b). Because Equation (8) indicates that λ_m depends on $|\langle \Psi_m^1 | \overline{H}_{S_0} | \Psi_n^3 \rangle|^2$ and $|\Delta E_{S_m-T_n}|$, the similar distribution shapes in Figure 6b,c indicate that $|\Delta E_{S_m-T_n}|$ does not cause the difference of k_p . Figure 6d shows the average of $\mu_{S_m \rightarrow S_0}^2 \lambda_m^2$ for all n of dimer 2. Because the two distinct peaks at $m = 9$ and 10 is observed in Figure 6d is similar to that in Figure 6b, the large $|\langle \Psi_m^1 | \overline{H}_{S_0} | \Psi_n^3 \rangle|^2$ of $m = 9$ and 10 accelerates k_p for $\text{Ge}(\text{C}_6\text{H}_5)_4$ crystals. The overall tendencies of dimer 2 presented in Figure 6a–d were also observed for the other dimers. In addition, the relationship between Figure 6a–d was observed when $\mu_{S_m \rightarrow S_0}^2$, $|\langle \Psi_m^1 | \overline{H}_{S_0} | \Psi_n^3 \rangle|^2$, λ_m^2 , and $\mu_{S_m \rightarrow S_0}^2 \lambda_m^2$ of dimer 1–5 were integrated (Figure S11, Supporting Information). Therefore, the large $|\langle \Psi_m^1 | \overline{H}_{S_0} | \Psi_n^3 \rangle|^2$ for $m = 9$ and 10 accelerates k_p of the $\text{Ge}(\text{C}_6\text{H}_5)_4$ crystals. Although it may be considered that the high-order excited state energies such as S_9 and S_{10} are too high, we note that the S_9-S_0 and $S_{10}-S_0$ energies are not much larger than the S_1-S_0 energy (Table S10, Supporting Information). Therefore, the moderate CT characteristics of S_m-S_0 transitions induced by degeneracy of HOMOs caused by highly symmetric π structures in addition to LE characteristics of the T_1-S_0 transition contribute to large $|\langle \Psi_m^1 | \overline{H}_{S_0} | \Psi_n^3 \rangle|^2$, which mainly causes the

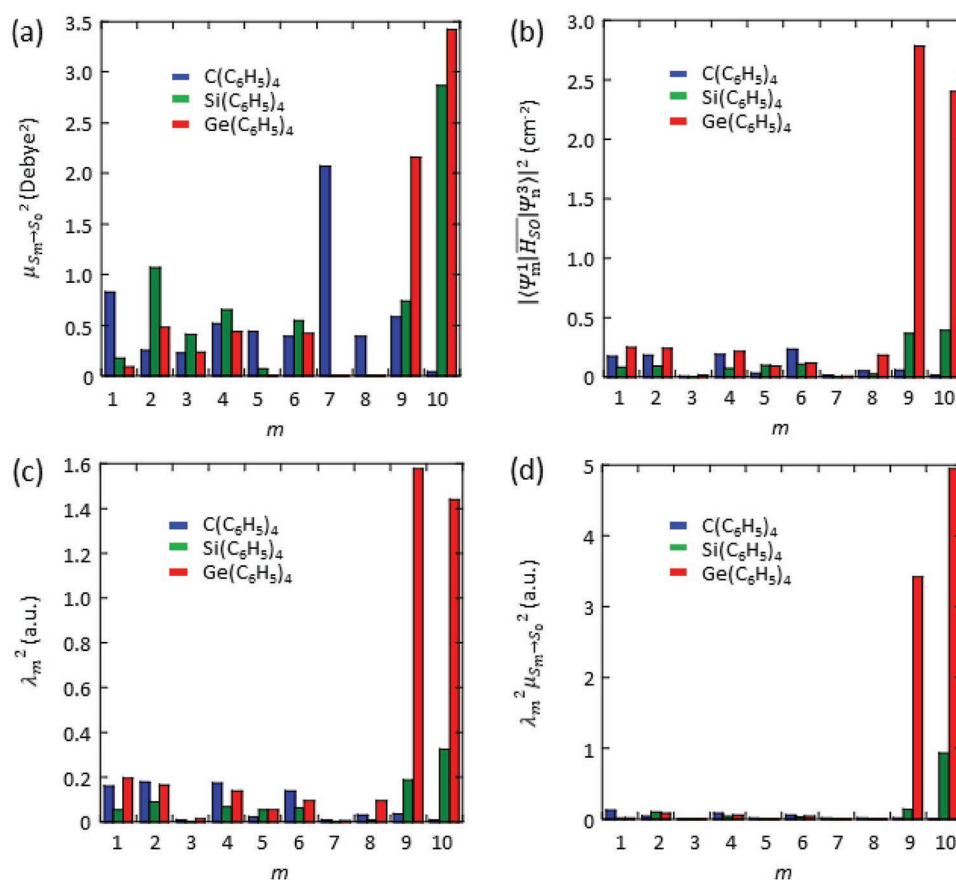


Figure 6. Relationships between photophysical parameters related to k_p and m of dimer 2 in $\text{C}(\text{C}_6\text{H}_5)_4$, $\text{Si}(\text{C}_6\text{H}_5)_4$, and $\text{Ge}(\text{C}_6\text{H}_5)_4$ crystals. Relationships between a) m and $\mu_{S_m \rightarrow S_0}^2$, b) m and $|\langle \Psi_m^1 | \overline{H}_{S_0} | \Psi_n^3 \rangle|^2$ averaged for $n = 1-8$, c) m and λ_m^2 averaged for $n = 1-8$, and d) m and $\mu_{S_m \rightarrow S_0}^2 \lambda_m^2$ averaged for $n = 1-8$.

increase of k_p independent of $k_{nr}(RT)$. This is an origin of the more efficient persistent RTP of $\text{Ge}(\text{C}_6\text{H}_5)_4$ crystals compared with that of $\text{C}(\text{C}_6\text{H}_5)_4$ and $\text{Si}(\text{C}_6\text{H}_5)_4$ crystals.

2.7. Roles of Local Electronic Structure in Achieving Efficient Persistent RTP

This investigation of k_p , $k_{nr}(RT)$, and $k_q(RT)$ considering the electronic structures of heavy atom-free aromatic crystals may provide us smooth strategies to explore highly efficient persistent RTP.

The suppression of the migration of triplet excitons at RT is necessary to minimize $k_q(RT)$ to realize large $\tau_p(RT)$ in crystals of heavy atom-free conjugated molecules. Small overlap of MOs related to hole and/or electron transfer between dimers in a crystalline structure is a way to obtain such suppression. A previous report^[59] revealed that CT conjugated molecules show strongly localized MOs, which sometimes minimizes the overlap of MOs and suppresses triplet exciton migration. This report proposes that the localization of MOs utilizing the π degeneracy of steric and highly symmetric conjugated structures is another way to sometimes minimize $k_q(RT)$ caused by triplet exciton diffusion. To suppress triplet exciton migration, effective separation of the HOMO and LUMO is necessary. However, the localization of both HOMO and LUMO is not suitable for persistent RTP because it causes large separation of HOMO and LUMO. Such separation results in rapid delayed fluorescence without persistent emission through rapid reverse ISC from T_1 to S_1 as a result of the very small energy difference between S_1 and T_1 . Strong CT characteristics of the T_1 - S_0 transition generally increase $\langle \Psi_0^{(0)} | \overline{H}_{SO} | \Psi_1^{(0)} \rangle$, as seen for benzophenone.^[18,56] Because this also increases the magnitude of the change of $\langle \Psi_0^{(0)} | \overline{H}_{SO} | \Psi_1^{(0)} \rangle$ depending on the change of coordinates of atoms (Q_p), i.e., VSOC, the CT characteristics of the T_1 - S_0 transition strongly increase $k_{nr}(RT)$. Conversely, $\langle \Psi_0^{(0)} | \overline{H}_{SO} | \Psi_1^{(0)} \rangle$ becomes small and VSOC also decreases when all triplet states near T_1 possess LE characteristics, resulting in small $k_{nr}(RT)$. Even when the HOMO or LUMO is strongly localized, the T_1 - S_0 transition still has moderate LE characteristics. Therefore, conjugated structures with a HOMO or LUMO that is strongly localized are candidate molecules for persistent RTP. When the T_1 - S_0 transition has LE character, introduction of moderate CT characteristics of the S_m - S_0 transition is effective. This report proposes that the localized MOs in some highly symmetric conjugated structures induce moderate CT characteristics in S_m - S_0 transitions.

From the above discussion, molecules with electronic structures that show strong localization of MOs involved in the T_1 - S_0 transition potentially contribute to the increase of k_p independent of $k_{nr}(RT)$ as well as minimization of $k_q(RT)$ to achieve efficient persistent RTP. However, appropriate molecular packing so that the localized MOs are separated is also crucial. Although prediction of crystalline packing is desirable, it is still very difficult. However, exploring molecular structures with strongly localized MOs is a way to increase the percentage of MOs with small overlap to minimize $k_q(RT)$. Thus, steric and highly symmetric conjugated structures in addition to moderate CT conjugated structures substituted with electron-donating or

-accepting substituents are candidates to meet the requirement of strongly localized MOs involved in the T_1 - S_0 transition. Because the electronic structure of a monomer can be predicted using current quantum calculations, prescreening of electronic structures may provide an approach to increase the percentage of prepared heavy atom-free conjugated crystals displaying efficient persistent RTP.

3. Conclusions

We examined the efficient persistent RTP from nonpolar and highly symmetric $\text{C}(\text{C}_6\text{H}_5)_4$, $\text{Si}(\text{C}_6\text{H}_5)_4$, and $\text{Ge}(\text{C}_6\text{H}_5)_4$ crystals in air. $\Phi_p(RT)$ of $\text{C}(\text{C}_6\text{H}_5)_4$, $\text{Si}(\text{C}_6\text{H}_5)_4$, and $\text{Ge}(\text{C}_6\text{H}_5)_4$ crystals in air were 3.1%, 5.1%, and 17%, respectively. $\tau_p(RT)$ of $\text{C}(\text{C}_6\text{H}_5)_4$, $\text{Si}(\text{C}_6\text{H}_5)_4$, and $\text{Ge}(\text{C}_6\text{H}_5)_4$ crystals in air were 1.10, 1.26, and 0.45 s, respectively. The appearance of crystallization-induced persistent RTP in air was caused by the large decrease of $k_{nr}(RT) + k_q(RT)$ upon crystallization rather than the increase of $\Phi_{isc}(RT)$. Quantum chemical calculations of factors related to Dexter type-electron exchange and the temperature dependence of $k_{nr}(T) + k_q(T)$ indicated that the small $k_{nr}(RT) + k_q(RT)$ is caused by the minimization of $k_q(RT)$ originating from the small diffusion length of triplet excitons in the crystals at RT. The small triplet diffusion length could be explained by inefficient hole transfer caused by the small overlap of HOMOs originating from HOMO localization, which is induced by the π degeneracy of the steric and highly symmetric molecular structure. The temperature dependence of $k_{nr}(RT) + k_q(RT)$ also indicated that $k_{nr}(RT)$ of $\text{C}(\text{C}_6\text{H}_5)_4$, $\text{Si}(\text{C}_6\text{H}_5)_4$, and $\text{Ge}(\text{C}_6\text{H}_5)_4$ crystals are small and do not contribute much to the decrease of $k_{nr}(RT) + k_q(RT)$. Analysis using VSOC considering vibration at RT supported the small contribution of $k_{nr}(RT)$ to the decrease of $k_{nr}(RT) + k_q(RT)$. While the increase of $k_{nr}(RT)$ of $\text{Ge}(\text{C}_6\text{H}_5)_4$ crystals was small compared with that of $\text{Si}(\text{C}_6\text{H}_5)_4$ crystals, k_p of $\text{Ge}(\text{C}_6\text{H}_5)_4$ crystals was 7.6 times larger than that of $\text{Si}(\text{C}_6\text{H}_5)_4$ crystals, which caused the large $\Phi_p(RT)$ of $\text{Ge}(\text{C}_6\text{H}_5)_4$ crystals. The large enhancement of k_p independent of the increase of $k_{nr}(RT)$ is mainly caused by the increase of SOC between the moderate CT characteristics of S_m - S_0 transitions and T_1 - S_0 transition with LE character. The moderate CT characteristics of S_m - S_0 transitions are induced by the HOMO localization in the highly symmetric conjugated structure of $\text{Ge}(\text{C}_6\text{H}_5)_4$. Thus, the localized HOMOs in highly symmetric conjugated structures play roles in acceleration of k_p independent of $k_{nr}(RT)$ as well as minimization of $k_q(RT)$.

In the last five years, a variety of heavy atom-free conjugated molecular crystals with persistent RTP have been reported. Our investigation indicates that persistent RTP of molecular crystals with small $\Phi_p(RT)$, like $\text{C}(\text{C}_6\text{H}_5)_4$ and $\text{Si}(\text{C}_6\text{H}_5)_4$ crystals, is obtained through small $k_q(RT)$ by suppression of triplet exciton migration at RT. Conversely, $\text{Ge}(\text{C}_6\text{H}_5)_4$ crystals showed increased k_p independent of $k_{nr}(RT)$ in addition to the large decrease of $k_q(RT)$. This is first overall analysis of k_p , $k_{nr}(RT)$, and $k_q(RT)$ of heavy atom-free conjugated molecular aggregates. The high simultaneous correlation between experimentally observed k_p , $k_{nr}(RT)$, and $k_q(RT)$ and those estimated from quantum chemical calculations suggests that a procedure to evaluate triplet excitons of heavy atom-free molecular aggregates is feasible. Because new aromatic

crystals showing persistent RTP and moderate $\Phi_p(\text{RT})$ have been reported recently, design of electronic structures that lead to $k_p > k_{nr}(\text{RT})$ without increase of $k_{nr}(\text{RT})$ is crucial to obtain highly efficient persistent RTP from heavy atom-free conjugated molecules under ambient conditions. Pre-screening using quantum chemical calculations focusing on moderate CT character of S_m and the localization of HOMO or LUMO will help researchers to find suitable electronic structures and materials. The enhancement of the characteristics of singlet and triplet states is important for developing new applications using persistent RT emission.

4. Experimental Section

$\text{C}(\text{C}_6\text{H}_5)_4$, $\text{Si}(\text{C}_6\text{H}_5)_4$, and $\text{Ge}(\text{C}_6\text{H}_5)_4$ powders were purified as Section 1 in the Supporting Information. XRD measurements of $\text{C}(\text{C}_6\text{H}_5)_4$, $\text{Si}(\text{C}_6\text{H}_5)_4$, and $\text{Ge}(\text{C}_6\text{H}_5)_4$ single crystals were performed at RT using a Bruker SMART APEX II ULTRA/CCD diffractometer. Absorption spectra of the samples were measured by an absorption spectrometer (V-760, Jasco International Co., Ltd., Japan). Fluorescence and persistent RTP spectra and $\tau_p(\text{T})$ were measured using a photonic multichannel analyzer (PMA-12, Hamamatsu Photonics, Japan) as a photodetector and an excitation unit of a fluorometer (FP-8300, Jasco International Co., Ltd.) as an excitation source. Persistent RTP spectra were collected by detecting emission spectra soon after ceasing excitation. $\Phi_r(\text{RT})$ and $\Phi_p(\text{RT})$ were determined using an absolute luminescence quantum yield measurement system (C9920-02G, Hamamatsu Photonics). The method described in the Supporting Information of an earlier study was used to determine $\Phi_p(\text{RT})$.^[12] The temperature used to determine the temperature dependence of $\tau_p(\text{RT})$ was controlled by a cryostat (Optistat-DNV, Oxford, United Kingdom). Fluorescence lifetime at RT was measured with a fluorescence lifetime spectrometer (C11367, Hamamatsu Photonics).

For calculations of k_p and VSOC, The SOC operator within the zeroth-order regular approximation (ZORA) was $\overline{H_{SO}}$ and the parameter $\langle \Psi_m^{(0)} | \overline{H_{SO}} | \Psi_n^{(0)} \rangle$ was treated as a perturbation based on the scalar relativistic orbitals. Values of $|\langle \Psi_m^{(0)} | \overline{H_{SO}} | \Psi_n^{(0)} \rangle|^2$ were expressed as sum of data between one singlet state and three kinds of triplet states with comparable excited energy. For quantum calculations of k_p , the molecular configurations that were determined by XRD of single crystals were used without structure optimization. Each k_p was treated as a perturbation based on the scalar relativistic orbitals. Hybrid-B3LYP and TZP were used as exchange-correlation functionals and the Slater-type all-electron basis set, respectively. To calculate VSOC, conformations including normal mode vibrations were optimized at T_1 using density functional theory (Gaussian09/B3LYP/6-31G(d)). Information about the SOC depending on each vibration in the conformations was treated as a perturbation based on the scalar relativistic orbitals. Hybrid-B3LYP and TZP were used in VSOC calculations as exchange-correlation functionals and the Slater-type all-electron basis set, respectively. $p_p(\text{RT}) = \langle \Psi_m^{(0)} | \overline{H_{SO}} | \Psi_n^{(0)} \rangle / \partial Q_p$ at each vibration was approximated according to the procedures reported in ref. [56]. To calculate transfer integrals, the molecular configurations that were determined by XRD of single crystals were used without structure optimization. GGA-PW91 and TZP were used as exchange-correlation functionals and the Slater-type all-electron basis set, respectively.

Supporting Information

Supporting Information is available from the Wiley Online Library or from the author.

Acknowledgements

The author thanks Suzukakedai Materials Analysis Division, Technical Department, Tokyo Institute of Technology, for XRD analysis. This work was supported by a program of Leading Initiative for Excellent Young Researchers (LEADER) from the Japan Society for the Promotion of Science (JSPS) and JSPS KAKENHI (Grant Nos. JP18H02046, JP18H04507, 26107014, and JP17K19152).

Conflict of Interest

The author declares no conflict of interest.

Keywords

aggregation induced emission, persistent room-temperature phosphorescence, spin-orbit coupling, transfer integral, triplet exciton diffusion

Received: February 21, 2019

Revised: March 21, 2019

Published online: May 10, 2019

- [1] M. A. Baldo, D. F. O'Brien, Y. You, A. Shoustikov, S. Sibley, M. E. Thompson, S. R. Forrest, *Nature* **1998**, 395, 151.
- [2] M. A. Baldo, S. Lamansky, P. E. Burrows, M. E. Thompson, S. R. Forrest, *Appl. Phys. Lett.* **1999**, 75, 4.
- [3] L. Flamigni, A. Barbieri, C. Sabatini, B. Ventura, F. Barigelletti, *Top. Curr. Chem.* **2007**, 281, 143.
- [4] A. J. Gareth Williams, *Top. Curr. Chem.* **2007**, 281, 205.
- [5] J. G. J. E. D. Dolmans, D. Fukumura, R. K. Jain, *Nat. Rev. Cancer* **2003**, 3, 380.
- [6] H. A. Collins, M. Khurana, E. H. Moriyama, A. Mariampillai, E. Dahlstedt, M. Balaz, M. K. Kuimova, M. Drobizhev, V. X. Yang, D. Phillips, A. Rebane, B. C. Wilson, H. L. Anderson, *Nat. Photonics* **2008**, 2, 420.
- [7] S. Zhang, M. Hosaka, T. Yoshihara, K. Negishi, Y. Iida, S. Tobita, T. Takeuchi, *Cancer Res.* **2010**, 70, 4490.
- [8] H. Kurokawa, H. Ito, M. Inoue, K. Tabata, Y. Sato, K. Yamagata, S. Kizaka-Kondoh, T. Kadonosono, S. Yano, M. Inoue, T. Kamachi, *Sci. Rep.* **2015**, 5, 10657.
- [9] D. B. Clapp, *J. Am. Chem. Soc.* **1939**, 61, 523.
- [10] V. B. Nazarov, V. I. Gerko, M. V. Alfimov, *Russ. Chem. Bull.* **1996**, 45, 969.
- [11] W. Z. Yuan, X. Y. Shen, H. Zhao, J. W. Y. Lam, L. Tang, P. Lu, C. Wang, Y. Liu, Z. Wang, Q. Zheng, J. Z. Sun, Y. Ma, B. Z. Tang, *J. Phys. Chem. C* **2010**, 114, 6090.
- [12] S. Hirata, K. Totani, J. Zhang, T. Yamashita, H. Kaji, S. R. Marder, T. Watanabe, C. Adachi, *Adv. Funct. Mater.* **2013**, 23, 3386.
- [13] Y. Deng, D. Zhao, X. Chen, F. Wang, H. Song, D. Shen, *Chem. Commun.* **2013**, 49, 5751.
- [14] X. Zhang, T. Xie, M. Cui, L. Yang, X. Sun, J. Jiang, G. Zhang, *ACS Appl. Mater. Interfaces* **2014**, 6, 2279.
- [15] Z. An, C. Zheng, Y. Tao, R. Chen, H. Shi, T. Chen, Z. Wang, H. Li, R. Deng, X. Liu, W. Huang, *Nat. Mater.* **2015**, 14, 685.
- [16] P. Xue, J. Sun, P. Chen, P. Wang, B. Yao, P. Gong, Z. Zhang, R. Lu, *Chem. Commun.* **2015**, 51, 10381.
- [17] X. Yang, D. Yan, *Adv. Opt. Mater.* **2016**, 4, 897.
- [18] J. N. Turro, *Modern Molecular Photochemistry*, University Science Books, Sausalito, California **1991**.

- [19] A. S. Mathew, C. A. DeRosa, J. N. Demas, C. L. Fraser, *Anal. Methods* **2016**, *8*, 3109.
- [20] K. Totani, Y. Okada, S. Hirata, M. Vacha, T. Watanabe, *Adv. Opt. Mater.* **2013**, *1*, 283.
- [21] S. Hirata, K. Totani, H. Kaji, M. Vacha, T. Watanabe, C. Adachi, *Adv. Opt. Mater.* **2013**, *1*, 438.
- [22] K. Jiang, L. Zhang, J. Lu, C. Xu, C. Cai, H. Lin, *Angew. Chem., Int. Ed.* **2016**, *55*, 7231.
- [23] P. Long, Y. Feng, C. Cao, Y. Li, J. Han, S. Li, C. Peng, Z. Li, W. Feng, *Adv. Funct. Mater.* **2018**, *28*, 1800791.
- [24] Y. Su, S. Z. F. Phua, Y. Li, X. Zhou, D. Jana, G. Liu, W. Q. Lim, W. K. Ong, C. Yang, Y. Zhao, *Sci. Adv.* **2018**, *4*, eaas9732.
- [25] Y. Gong, G. Chen, Q. Peng, W. Z. Yuan, Y. Xie, S. Li, Y. Zhang, B. Z. Tang, *Adv. Mater.* **2015**, *27*, 6195.
- [26] C. Li, X. Tang, L. Zhang, C. Li, Z. Liu, Z. Bo, Y. Q. Dong, Y. H. Tian, Y. Dong, B. Z. Tang, *Adv. Opt. Mater.* **2015**, *3*, 1184.
- [27] Y. Katsurada, S. Hirata, K. Totani, T. Watanabe, M. Vacha, *Adv. Opt. Mater.* **2015**, *3*, 1726.
- [28] J. Yang, X. Zhen, B. Wang, X. Gao, Z. Ren, J. Wang, Y. Xie, J. Li, Q. Peng, K. Pu, Z. Li, *Nat. Commun.* **2018**, *9*, 840.
- [29] L. Gu, H. Shi, M. Gu, K. Ling, H. Ma, S. Cai, L. Song, C. Ma, H. Li, G. Xiag, X. Hang, J. Li, Y. Go, W. Yao, Z. Shuai, Z. An, X. Liu, W. Huang, *Angew. Chem., Int. Ed.* **2018**, *57*, 8425.
- [30] X. Zhen, Y. Tao, Z. An, P. Chen, C. Xu, R. Chen, W. Huang, K. Pu, *Adv. Mater.* **2017**, *29*, 1606665.
- [31] S. M. A. Fateminia, Z. Mao, S. Xu, Z. Yang, Z. Chi, B. Liu, *Angew. Chem., Int. Ed.* **2017**, *56*, 12160.
- [32] G. N. Lewis, D. Lipkin, T. T. Magel, *J. Am. Chem. Soc.* **1941**, *63*, 3005.
- [33] D. F. Evans, *Nature* **1955**, *176*, 777.
- [34] P. F. Jones, S. Siegel, *J. Chem. Phys.* **1969**, *50*, 1134.
- [35] J. L. Kropp, W. R. Dawson, *J. Phys. Chem.* **1967**, *71*, 4499.
- [36] G. Zhang, J. Chen, S. J. Payne, S. E. Kooi, J. N. Demas, C. L. Fraser, *J. Am. Chem. Soc.* **2007**, *129*, 8942.
- [37] G. Zhang, G. L. Fiore, T. L. S. Clair, C. L. Fraser, *Macromolecules* **2009**, *42*, 3162.
- [38] H. A. Al-Attar, A. P. Monkman, *Adv. Funct. Mater.* **2012**, *22*, 3824.
- [39] S. Hirata, M. Vacha, *J. Phys. Chem. Lett.* **2016**, *7*, 1539.
- [40] S. Hirata, M. Vacha, *Adv. Opt. Mater.* **2017**, *5*, 1600996.
- [41] X. Ma, C. Xu, J. Wang, H. Tian, *Angew. Chem.* **2018**, *130*, 11020.
- [42] J. Wei, B. Liang, R. Duan, Z. Cheng, C. Li, T. Zhou, Y. Yi, Y. Wang, *Angew. Chem., Int. Ed.* **2016**, *55*, 15589.
- [43] H. Mieno, R. Kabe, N. Notsuka, M. D. Allendorf, C. Adachi, *Adv. Opt. Mater.* **2016**, *4*, 1015.
- [44] Q. Li, M. Zhou, Q. Yang, Q. Wu, J. Shi, A. Gong, M. Yang, *Chem. Mater.* **2016**, *28*, 8221.
- [45] Q. Li, M. Zhou, M. Yang, Q. Yang, Z. Zhang, J. Shi, *Nat. Commun.* **2018**, *9*, 734.
- [46] Z. Yang, Z. Mao, X. Zhang, D. Ou, Y. Mu, Y. Zhang, C. Zhao, S. Liu, Z. Chi, J. Xu, Y. C. Wu, P. Y. Lu, A. Lien, M. R. Bryce, *Angew. Chem., Int. Ed.* **2016**, *55*, 2181.
- [47] M. Shimizu, R. Shigitani, M. Nakatani, K. Kuwabara, Y. Miyake, K. Tajima, H. Sakai, T. Hasobe, *J. Phys. Chem. C* **2016**, *120*, 11631.
- [48] W. Zhao, Z. He, J. W. Y. Lam, Q. Peng, H. Ma, Z. Shuai, G. Bai, J. Hao, B. Z. Tang, *Chem* **2016**, *1*, 592.
- [49] S. Kuno, H. Akeno, H. Ohtani, H. Yuasa, *Phys. Chem. Chem. Phys.* **2015**, *17*, 15989.
- [50] S. Kuno, T. Kanamori, Z. Yijing, H. Ohtani, H. Yuasa, *ChemPhotoChem* **2017**, *1*, 102.
- [51] Y. Xie, Y. Ge, Q. Peng, C. Li, Q. Li, Z. Li, *Adv. Mater.* **2017**, *29*, 1606829.
- [52] L. Bian, H. Shi, X. Wang, K. Ling, H. Ma, M. Li, Z. Cheng, C. Ma, S. Cai, Q. Wu, N. Gan, X. Xu, Z. An, W. Huang, *J. Am. Chem. Soc.* **2018**, *140*, 10734.
- [53] Y. Yang, K. Wang, D. Yan, *ACS Appl. Mater. Interfaces* **2016**, *8*, 15489.
- [54] X. Chen, W. Luo, H. Ma, Q. Peng, W. Z. Yuan, Y. Zhang, *Sci. China: Chem.* **2018**, *61*, 351.
- [55] X. Dou, Q. Zhou, X. Chen, Y. Tan, X. He, P. Lu, K. Sui, B. Z. Tang, Y. Zhang, W. Z. Yuan, *Biomacromolecules* **2018**, *19*, 2014.
- [56] S. Hirata, *J. Phys. Chem. Lett.* **2018**, *9*, 4251.
- [57] S. Xu, R. Chen, C. Zheng, W. Huang, *Adv. Mater.* **2016**, *28*, 9920.
- [58] S. Hirata, *Adv. Opt. Mater.* **2017**, *5*, 1700116.
- [59] K. Narushima, Y. Kiyota, T. Mori, S. Hirata, M. Vacha, *Adv. Mater.* **2019**, *31*, 1807268.
- [60] S. Hirata, K. Totani, T. Yamashita, C. Adachi, M. Vacha, *Nat. Mater.* **2014**, *13*, 938.
- [61] S. Hirata, M. Vacha, *Adv. Opt. Mater.* **2016**, *4*, 297.
- [62] J. Kujit, F. Ariese, U. A. Brinkman, C. Gooijer, *Anal. Chim. Acta* **2003**, *488*, 135.
- [63] K. Mori, T. P. M. Goumans, E. van Lenthe, F. Wang, *Phys. Chem. Chem. Phys.* **2014**, *16*, 14523.
- [64] G. L. Closs, M. D. Johnson, J. R. Miller, P. Piotrowiak, *J. Am. Chem. Soc.* **1989**, *111*, 3751.
- [65] M. S. Kwon, Y. Yu, C. Coburn, A. W. Phillips, K. Chung, A. Shanker, J. Jung, G. Kim, K. Pipe, S. R. Forrest, J. H. Youk, J. Gierschner, J. Kim, *Nat. Commun.* **2015**, *6*, 8947.
- [66] S. Hirata, M. Vacha, *J. Phys. Chem. Lett.* **2017**, *8*, 3683.
- [67] G. M. Akselrod, P. B. Deotare, N. J. Thompson, J. Lee, W. A. Tisdale, M. A. Baldo, V. M. Menon, V. Bulović, *Nat. Commun.* **2014**, *5*, 3646.
- [68] S. Eldin, J. F. Liebman, L. D. Reynolds, P. Dowd, *Tetrahedron Lett.* **1992**, *33*, 4525.
- [69] F. Metz, S. Friedrich, G. Hohlneicher, *Chem. Phys. Lett.* **1972**, *16*, 353.
- [70] F. Metz, *Chem. Phys. Lett.* **1973**, *22*, 186.
- [71] H. Gropper, F. Dörr, *Ber. Bunsenges. Phys. Chem.* **1963**, *67*, 46.
- [72] M. A. El-Sayed, *J. Chem. Phys.* **1963**, *38*, 2834.